A distributed space radar sounder using a cross-track flying tethered satellite system

Acta Astronautica 221 (2024) 266–282

Contents lists available at ScienceDirect

Acta Astronautica

journal homepage: www.elsevier.com/locate/actaastro

# A distributed space radar sounder using a cross-track flying tethered satellite system

Stefano Aliberti [a,*], Marco B. Quadrelli [b], Marcello Romano [a]

[a] Astrodynamics and Advanced Orbital Systems (ASTRADORS) Laboratory, Department of Mechanical & Aerospace Engineering, Politecnico di Torino, Corso Duca degli Abruzzi, 24, 10129, Turin, Italy

[b] Jet Propulsion Laboratory, California Institute of Technology, 4800 Oak Grove Drive, Pasadena, CA, 91109-8099, USA

ARTICLE INFO

*Keywords:*
Radar remote sensing
Distributed radar sounders
Tethered satellite systems
Distributed space systems
Aerodynamic control

ABSTRACT

The objective of this paper is to analyze the performance of two possible architectures of tethered satellite systems, used as a platform for a distributed radar sounder. The first architecture consists in a cross-track oriented tethered satellite system, controlled and stabilized by exploiting the aerodynamic forces generated by the interaction with the rarefied atmosphere in Low Earth Orbit. The second architecture involves a tethered satellite system controlled through gyroscopic stabilization, obtained by spinning the system about an axis contained in the orbital plane. After a brief survey of radar sounding techniques, the methodology is introduced for describing the geometry of the systems and their characteristics, the performance of the two architectures are then compared with each other and with the current state of the art. By analyzing the modeled nominal behavior, it is shown that the two proposed architectures can achieve continuous or multiple observations, respectively, at maximum cross-track resolution, during one orbit, minimizing clutter noise. This is a considerable improvement of performance versus a formation flight architecture which can typically achieve only up to four observations per orbit. Finally, the advantages and disadvantages of each architecture are studied, and their possible mission scenarios are discussed.

## 1. Introduction

Space-based radar sounders are low-frequency ground-penetrating radars, operating from orbit and used to inspect planetary sub-surfaces. By orbiting around a celestial body (e.g., Earth, Mars, Venus, etc.), these systems benefit from a privileged point of view, and are able to potentially observe any point on the surface. Classic spaceborne radar sounders consists in an antenna mounted on a single orbiting satellite. As the satellite moves along its orbit (i.e., in the along-track direction), it acquires several measurements of the same target, that are combined by using synthetic aperture data-processing techniques [1]. Significant examples of this technology are the Apollo 17 Lunar Sounder Experiment (ALSE), which analyzed the lunar subsurface as part of the Apollo missions [2], the Mars Advanced Radar for Subsurface and Ionosphere Sounding (MARSIS) mission, that aimed to find water in the subsurface of Mars [3], and the Selenological and Engineering Explorer (SELENE) mission, whose goal was to study the origin of the Moon and its geological evolution [4]. Recent studies have proposed to increase the performance of these systems by using formation flying satellites. Specifically, it is possible to increase cross-track resolution, signal-to-noise ratio (SNR) and reduce clutter noise by using formations of satellites that are distributed in the cross-track direction (i.e., perpendicular to the along-track and radial direction) [5]. However, in these cases, the evolution in time of the cross-track aperture is constrained by the orbital dynamics and by the necessarily limited use of propellant. Moreover, a precise knowledge of the relative position between the satellites of the formation is required in order to properly process the signal. Formation flying architectures require very frequent corrections to counteract the external perturbations and ensure the desired performance, and complex satellites are needed to perform accurate maneuvers [6]. The here proposed use of a Tethered Satellite System (TSS) represents an alternative and potentially advantageous solution. By mechanically linking the satellites that make up the distributed space system, the propellant consumption for formation keeping is reduced or even zeroed out. The study of space tether for remote sensing missions is not new. For instance, Moccia et al. hypothesized the use of a tethered architecture mounted on the Space Shuttle for Interferometric Synthetic Aperture Radar [7,8], while more recent studies have investigated the potential performance of an end-fire array based on a radial tethered satellite system for radar sounding application [9,10]. These architectures, however, are limited to the use

* Corresponding author.
*E-mail addresses:* stefano.aliberti@polito.it (S. Aliberti), marco.b.quadrelli@jpl.nasa.gov (M.B. Quadrelli), marcello.romano@polito.it (M. Romano).

https://doi.org/10.1016/j.actaastro.2024.05.018
Received 15 February 2024; Received in revised form 23 April 2024; Accepted 11 May 2024
Available online 14 May 2024

**Nomenclature**

| | |
|---|---|
| $B_D$ | Doppler Bandwidth [Hz] |
| $B_w$ | Bandwidth [Hz] |
| $d_{at}$ | Distance in the along-track direction [m] |
| $d_{ct}$ | Distance in the cross-track direction [m] |
| $d_p$ | Line of sight distance between sensors [m] |
| $d_r$ | Distance in the radial direction [m] |
| $f_D$ | Doppler frequency [Hz] |
| $h$ | Sensor altitude [m] |
| $IRF$ | Cross-track improvement resolution factor [–] |
| $k$ | Wavenumber of the harmonic field [$m^{-1}$] |
| $L$ | Tether length [m] |
| $L_{at}$ | Along-track equivalent antenna length [m] |
| $L_{ct}$ | Cross-track equivalent antenna length [m] |
| $N$ | Total number of sensors [–] |
| $PRI$ | Pulse repetition interval [s] |
| $R_{ct}$ | Cross-track resolution [m] |
| $T_i$ | Integration time [s] |
| $V_s$ | Sensor orbital velocity [m/s] |
| $\alpha$ | In-plane angle [rad] |
| $\beta$ | Out-of-plane angle [rad] |
| $\Delta\phi$ | Phase correction [–] |
| $\theta_p$ | Array rotation angle [deg] |
| $\theta_b$ | Cross-track equivalent beamwidth [deg] |
| $\theta_g$ | Angular position of the first grating lobe [deg] |
| $\theta_{err}$ | Pointing error [deg] |
| $\lambda$ | Radar wavelength [m] |
| $\mu$ | Gravitational parameter [$km^3/s^2$] |
| $\omega$ | Tether rotational speed [rad/s] |
| $\Omega$ | Orbit mean motion [rad/s] |

of a radial tether, stabilized by gravity gradient. Recent studies have shown that it is possible to stabilize a linear tethered satellite system in other configurations than the (naturally stable) radial one [11], through the use of the gyroscopic effect [12–15], or the use of aerodynamic effects [16,17]. The main original contributions of the present paper are:

1. Analysis of the possible radar-sounding performance of aerodynamically and gyroscopically stabilized tethered satellite systems;
2. Comparison of the performances of those two architectures, formation-flying solution, and a single-satellite solution.
3. The introduction of a phase correction to ensure any-attitude nadir pointing for gyroscopic TSS.

The paper is organized as follows.

Section 2 surveys spaceborne Synthetic Aperture Radar (SAR) systems, and their applications. Section 3, outlines the principles of radar sounding, highlighting the most important equations for calculating the performance of single-satellite and distributed systems. Section 4 introduces the mission geometry, the model of a linear tether satellite system and the mathematical tools to describe its performance and pointing. Section 5 studies the aerodynamically stabilization. Section 6 studies the gyroscopic stabilization. In Section 7 the two tethered architectures are compared to a formation flying and a single-satellite architectures, and their performances are analyzed. Section 8 discusses the results. Finally, in Section 9, concludes the paper.

## 2. Brief survey of spaceborne synthetic aperture radar techniques

Synthetic Aperture Radar (SAR) is an active microwave remote sensing technique that exploits the relative motion between an antenna and a target in order to increase the performance (e.g., the resolution) of a given instrumentation. A SAR system emits a sequence of electromagnetic pulses while moving above a target, and collect and analyzes the amplitude, phase, frequency and time delay of the signal that echoes back. By knowing the relative motion of the antenna with respect to the target, the information pertaining to the different pulses are processed in such a way that a synthetic equivalent antenna aperture is obtained, that spans up to several kilometers. Different solutions can be implemented in order to obtain a moving platform for the antenna: e.g., a single antenna that irradiates a target in a direction perpendicular to the fly-path, and is mounted on an aircraft (airborne SAR) or on a spacecraft (Spaceborne SAR). Spaceborne SAR, object of this study, have been used since the 1970's for Earth and planetary exploration. According to the probing wavelength, SAR systems have different applications including:

- **X-Band** (frequency: 8–12 GHz, wavelength: 3.8–2.4 cm) is generally used for high resolution imaging and ice monitoring, but presents a low penetration capability into vegetation cover. Examples include: SAR-Lupe [18], COSMO-SkyMed [19], TerraSAR-X/TanDem-X [20] and PAZ [21].
- **C-Band** (frequency: 4–8 GHz, wavelength: 7.5–3.8 cm) is generally used for global mapping and change detection. Examples include: ERS-1/2 [22], RadarSAT-1 [23], RadarSAT-2 [24] and RadarSAT - Constellation [25].
- **S-Band** (frequency: 2–4 GHz, wavelength: 15–7.5 cm) is mainly used for Earth observation and agriculture data collection. An example is the SAR-S mounted on the HJ-1-C satellite [26].
- **L-Band** (frequency: 1–2 GHz, wavelength: 30–15 cm) is generally used for geophysical monitoring, biomass and vegetation mapping, Interferometric Synthetic Aperture Radar (InSAR). This band was used for the first SAR for Earth observation mounted on SeaSat [27], for J-ERS [28], and in PALSAR [29].
- **P-band** (frequency: 0.3–1 GHz, wavelength: 1–0.3 m) is particularly suitable for vegetation mapping and assessment. Biomass, the first P-band spaceborne SAR, will be launched in 2024 [30]
- **VHF-HF** (frequency: 3–300 MHz, wavelength: 100–1 m) is used for penetrative radar and radar sounder applications. Signals in this frequency range can penetrate into the ground, so that information about the composition and structure of the subsurface can be obtained. Some examples include: ALSE [2], RIME [31],LRS (SELENE) [4], SRS (EnVision) [32], SHARAD [33], MARSIS [3]

Tables 1 and 2 list, in a chronological order, selected missions that have employed SAR techniques. The items marked in bold refer to radar sounding missions, the subject of this paper.

## 3. Fundamentals of radar sounding

Radar sounding is a geophysical method that uses radar pulses to image the subsurface of a planet. Radar sounders are based on the transmission of electromagnetic pulses in the range of midfrequency (MF), high-frequency (HF) or very high-frequency (VHF) from a moving platform (generally airborne or spaceborne). The electromagnetic pulses, transmitted toward the surface and subsurface of the planet, are reflected, generating echoes that are detected and processed. Through the analysis of these data, important information on subsurface composition and surface characteristics can be deduced [1]. These systems have the best performance in Radioglaciology applications, since ice is particularly transparent at these frequencies, but with shallower penetration depths they can also be used for different types of subsurface, providing information on soil moisture and the interface between different subsurface layers. Relevant examples of the application of

**Table 1**
Spaceborne synthetic aperture radar missions (Part. 1)

| Lifetime | Mission | Band | Purpose | Ref. |
|---|---|---|---|---|
| 1972 | **ALSE** (Apollo 17) | HF (5–15 MHz)<br>VHF (150 MHz) | Ground penetrating radar, used to study Moon's surface and interior down to 2 km. | [2] |
| 1978 | SeaSat | L-band (1.275 GHz) | Oceanography: study sea-surface winds and temperature, wave's features and ocean topography. | [27] |
| 1991–2000<br>1995–2011 | ERS-1/2 | C-Band (5.30 GHz) | Earth imaging (image-mode) and oceanography (wave-mode). | [22] |
| 1992–1998 | J-ERS-1 | L-band (1.275 GHz) | Multi-purpose imagery, analyze Earth surface albedo and reflectance, sea ice and snow cover, edge and depths, landscape topography and vegetation. | [28] |
| 1994 | SIR-C/X-SAR<br>(STS-58/69) | L-band (1.250 GHz)<br>C-band (5.3 GHz)<br>X-band (9.6 GHz) | SAR multi-frequency imagery for geology, hydrology, ecology and oceanography studies. | [34] |
| 1995–2013 | RadarSAT-I | C-band (5.3 GHz) | Earth imagery for scientific and commercial purposes. | [23] |
| 2000 | SRTM (STS-99) | C-band (5.3 GHz)<br>X-band (9.6 GHz) | Near-global topographic map of Earth (C-band) and slightly higher resolution image without global coverage (X-band). | [35] |
| 2002–2012 | ASAR (Envisat) | C-band (5.331 GHz) | Study of the ocean, such as waves, sea ice extent and motion, and land surface studies, such as deforestation and ground movement. | [36] |
| 2005-now | **MARSIS** (Mars Express) | MF-HF (1.8–5 MHz) | Search for water in the Martian sub-surface (down to 15 km). Characterize the surface elevation, roughness, and radar reflectivity of the planet. | [3] |
| 2006-now | **SHARAD**<br>(Mars Reconnaissance Orbiter) | HF (20 MHz) | Mapping the first kilometer below the Mars surface, providing images of subsurface scattering layers with high vertical resolution (15 m). | [33] |
| 2006–2011 | PALSAR (ALOS) | L-band (1.270 GHz) | Acquisition of data beneficial to resource exploration and environmental protection. | [29] |
| 2006–2008 | SAR-Lupe | X-band (9.65 GHz) | High-resolution radar imagery for defense-related purpose. | [18] |

these systems are the MARSIS mission, which revealed the presence of ice and liquid water in the Martian subsurface [3], and the Apollo Lunar Sounder Experiment (ALSE), that provided important information about the lunar subsurface [2].

### 3.1. Single sounder architecture

Classical radar sounder architectures exploit the orbital movement of a satellite in the along-track direction, in order to synthesize a large virtual aperture by using synthetic aperture processing. The synthetic aperture is achieved by exploiting the Doppler effect (i.e., the change in the frequency caused by the movement of the source with respect to a receiver). The relative displacement between the satellite and the target, causes a continuous Doppler shift of the echo coming from the target. By predicting the frequency shift, it is possible to identify different targets in the same scene, increasing the along-track resolution. It is possible to distinguish between focused and unfocused Doppler processing. In the first case, the phase history during the acquisition is exploited to maximize the along track resolution, up to the order of a few meters. This strategy needs high computational effort and is power demanding [1]. Unfocused processing employs a linear phase compensation, which can be easily implemented on board, but, on the other hand, it achieves lower along-track resolution. The along-track synthetic antenna length $L_{at}$ is defined as the space covered by the satellite during an acquisition. For a focused Doppler processing, the focused synthetic antenna length $L_{at}^{f}$ is limited by the far-field condition: in order to consider a coherent scatter, the ray hitting the target shall be parallel during the entire acquisition. In order to satisfy this condition, the maximum phase shift during the acquisition should be lower than $\pi/2$, equivalent to a maximum variation of the distance between satellite and target equal to $\lambda/4$ (Fig. 1)

$$d_{max} - d_{min} = \sqrt{\left(\frac{L_{at}^{f}}{2}\right)^{2} + h^{2}} - h \leq \frac{\lambda}{4} , \tag{1}$$

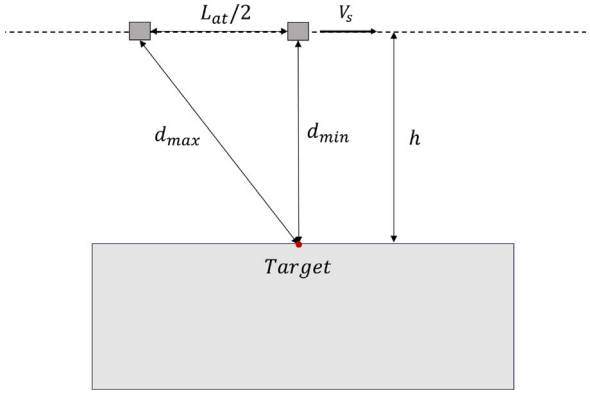


**Fig. 1.** Illustration of geometric considerations for obtaining synthetic antenna length for a focused Doppler processing (not in scale).

that can be re-arranged as

$$\sqrt{\left(\frac{L_{at}^{f}}{2h}\right)^{2} + 1} - 1 \leq \frac{\lambda}{4h} , \tag{2}$$

considering $L_{at}^{f} \ll h$, let us introduce the second-order Taylor series, which yields to

$$1 + \frac{1}{2}\left(\frac{L_{at}^{f}}{2h}\right)^{2} - 1 \leq \frac{\lambda}{4h} , \tag{3}$$

that gives the final expression

$$L_{at}^{f} < \sqrt{2\lambda h} . \tag{4}$$

**Table 2**
Spaceborne synthetic aperture radar missions (Part. 2)

| Lifetime | Mission | Band | Purpose | Ref. |
|---|---|---|---|---|
| 2007-now | RadarSAT-II | C-band (5.405 GHz) | Ice and environmental monitoring, marine surveillance, disaster management, resource management and mapping. | [24] |
| 2007–2009 | **LRS** (SELENE) | HF (5 MHz) | Sounding the surface and subsurface structures (down to 5 km) of the Moon. | [37] |
| 2007-now<br>2010-now | TerraSAR-X<br>TanDEM-X | X-band (9.65 GHz) | Earth radar imaging and development of a high accuracy Digital Elevation Model. | [20] |
| 2007–2010 | COSMO-SkyMed | X-band (9.6 GHz) | Emergency prevention, defense, scientific and commercial purposes. | [19] |
| 2013–2022 | KOMpsat-5 | X-band (9.66 GHz) | Imaging for the monitoring of environmental disasters. | [38] |
| 2013–2022 | SAR-S (HJ-1-C) | S-band (3.13 GHz) | High spatial resolution imaging. | [26] |
| 2012–2016 | RISAT-1 | C-band (5.35 GHz) | Natural resources management (agriculture planning, forestry survey), predict and prevent flooding. | [39] |
| 2014-now<br>2016–2021 | SENTINEL-1a<br>SENTINEL-1b | C-band (5.405 GHz) | Sea and land monitoring, emergency response to environmental disasters, and economic applications. | [40] |
| 2014-now | ALOS-2 | L-band (1.2575 GHz) | Monitoring of Japanese natural disasters, land and agriculture, and explores natural resources in the ground and seabed. | [41] |
| 2018-now | PAZ | X-band (9.65 GHz) | Provide imagery for both civilian, security and defense requirements. | [21] |
| 2019-now | Radarsat Constellation 1–3 | C-band (5.405 GHz) | Provide data for climate research and commercial applications including oil exploration, fishing, shipping. | [25] |
| 2023-now | **RIME**<br>(Jupiter Icy Moons Explorer) | HF (9 MHz) | Study the subsurface structure of Jovian moons down to 9 km. | [31] |
| 2024 (planned) | Biomass | P-band (0.435 GHz) | Monitoring of forests and vegetation. | [30] |
| 2031 (planned) | **SRS** (EnVision) | HF (9-30 MHz)<br>S-band (3.2 GHz) | Investigate Venus subsurface material boundaries in various geological terrains (HF) and provide several imaging and ranging techniques from a polar orbit (S-band). | [32] |

For an unfocused Doppler processing, the synthetic aperture is obtained by considering a linear change in Doppler frequency. This approximation is valid as long as the signal phase variation $\Delta\phi$ is lower than $\pi/4$. The two-way phase shift between the transmitted and received signal is

$$\phi = -2\pi\frac{2d}{\lambda} = -\frac{4\pi d}{\lambda}\ , \tag{5}$$

the maximum of the phase variation can be obtained comparing the nearest and farthest point of the acquisition

$$(\Delta\phi)_{max} = \frac{4\pi d_{max}}{\lambda} - \frac{4\pi d_{min}}{\lambda} < \frac{\pi}{4}\ . \tag{6}$$

By considering that the unfocused synthetic aperture extends for $L_{at}^{uf}$, it yields

$$d_{max} = \sqrt{\left(\frac{L_{at}^{uf}}{2}\right) + h^2}\ , \qquad d_{min} = h\ , \tag{7}$$

with

$$\sqrt{\left(\frac{L_{at}^{uf}}{2h}\right)^2 + 1} - 1 < \frac{\lambda}{16h}\ , \tag{8}$$

and, for $L_{at}^{uf} \ll h$, by introducing the second-order Taylor series, yields to

$$L_{at}^{uf} < \sqrt{\frac{\lambda h}{2}}\ . \tag{9}$$

Furthermore, it is possible to define the integration time $T_i$ as the time needed by the satellite to span the distance $L_{at}$

$$T_i = \frac{L_{at}}{V_s}\ , \tag{10}$$

where $V_s$ is the velocity of the satellite. For a circular orbit and assuming a spherical primary body, the altitude $h$ is constant, and the orbital velocity is equal to

$$V_s = \sqrt{\frac{\mu}{R+h}}\ , \tag{11}$$

where $\mu$ is the gravitational parameter and $R$ the radius of the primary body. The total Doppler bandwidth $B_D$ can be calculated considering the variation in Doppler frequency $f_D$. This can be computed as

$$\begin{aligned} f_D(t) &= \frac{1}{2\pi}\frac{\partial}{\partial t}\phi \\ &= \frac{1}{2\pi}\frac{\partial}{\partial t}\left(-\frac{4\pi d(t)}{\lambda}\right) \\ &= -\frac{2}{\lambda}\frac{\partial}{\partial t}d(t)\ . \end{aligned} \tag{12}$$

Considering that

$$d(t) = \sqrt{h^2 + (V_s t)^2} \approx h + \frac{V_s^2 t^2}{2h}\ , \tag{13}$$

with

$$-\frac{T_i}{2} < t < \frac{T_i}{2}\ , \tag{14}$$

it yields

$$f_D(t) = -\frac{2V_s^2 t}{h\lambda}\ . \tag{15}$$

The total Doppler bandwidth can be computed as the difference between the higher and lower Doppler frequency

$$B_D = f_D(t = T_i/2) - f_D(t = -T_i/2) = \frac{2V_s^2 T_i}{h\lambda} . \tag{16}$$

Both for the focused and unfocused Doppler processing, the total Doppler bandwidth can be calculated as a function of the synthetic aperture $L_{at}$

$$B_D^f = \frac{2V_s L_{at}^f}{h\lambda} , \qquad B_D^{uf} = \frac{2V_s L_{at}^{uf}}{h\lambda} . \tag{17}$$

The relative along-track resolution is

$$R_{at} \approx \frac{V_s}{B_D} = \frac{h\lambda}{2L_{at}} . \tag{18}$$

So, it is possible to define the different along-track resolution for the focused and unfocused Doppler processing

$$R_{at}^f = \frac{1}{2}\sqrt{\frac{h\lambda}{2}} , \qquad R_{at}^{uf} = \sqrt{\frac{h\lambda}{2}} . \tag{19}$$

This shows that with a focused Doppler algorithm it is possible to achieve an along-track resolution two times higher than the unfocused processing. In order to properly sample the Doppler frequencies, it is fundamental to use a Pulse Repetition Interval (PRI) adequately brief. The Doppler bandwidth defines the lower limit of the Pulse Repetition Frequency (PRF), that is the inverse of the Pulse Repetition Interval

$$PRF = \frac{1}{PRI} > B_D . \tag{20}$$

In the cross-track direction, on the other hand, there is not any relative motion between the sensor and the target. For this reason, no Doppler processing is possible, and the resolution is limited by the physical size of the antenna. For an isotropic antenna the resolution is limited by the first pulse-limited resolution cell $D_{pl}$ [1]

$$R_{ct}^s = D_{pl} = 2\sqrt{\frac{hc_o}{B_w}} , \tag{21}$$

where $B_w$ is the bandwidth and $c_o$ the speed of light in vacuum. In order to measure the distance between the sensor and the region in the subsurface that generates an echo, a radar sensor measures the time intervals occurring between the signal transmission and its reception. Let us now consider that the maximum expected penetration depth is $z_p$. The time required for the electromagnetic radiation to reach depth $z_p$ and return back is

$$\Delta t = 2\left(\Delta t_1 + \Delta t_2\right) = 2\left(\frac{h}{c_o} + \frac{z_p}{c_r}\right) , \tag{22}$$

where $c_o$ is the speed of the light in the vacuum and $c_r$ is the speed of the light in the subsurface. By indicating with $\varepsilon_r$ the subsurface dielectric constant, the speed of the light in the subsurface can be expressed as

$$c_r = \frac{c_o}{\sqrt{\varepsilon_r}} . \tag{23}$$

By introducing Eq. (23) in Eq. (22) it yields

$$\Delta t = \frac{2}{c_o}\left(h + \sqrt{\varepsilon_r} z_p\right) . \tag{24}$$

$\Delta t$ indicates the maximum time window within which the echo of the sent signal returns to the receiver. During this time window, however, in addition to the useful data caused by the echo of the signal penetrating to the satellite's nadir, the receiver will detect the echo of the waves sent over a spherical horizon whose radius is equal to

$$c_o \frac{\Delta t}{2} = h + \sqrt{\varepsilon_r} z_p . \tag{25}$$

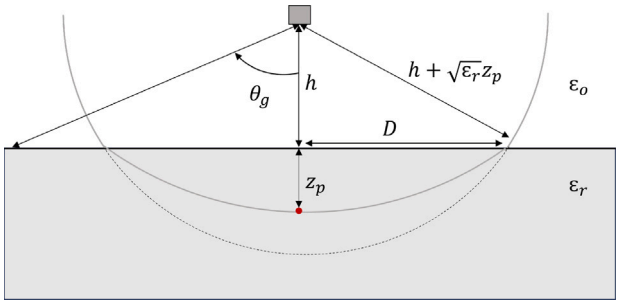


**Fig. 2.** Illustration of geometric considerations for obtaining the useful sounding scene of an acquisition (not in scale).

With simple geometrical considerations, through the intersection of a sphere of radius $h + \sqrt{\varepsilon_r} z_p$ and the ground, it is possible to obtain the radius of the useful sounding scene $D$ (Fig. 2)

$$D = \sqrt{(h + \sqrt{\varepsilon_r} z_p)^2 - h^2} . \tag{26}$$

Electromagnetic waves hitting the useful sounding scene will be reflected by the surface and can be disguised as subsurface echoes (i.e., clutter noise), worsening the performance of the acquisition.

### 3.2. Distributed radar sounder

A distributed radar sounder is an architecture that employs multiple satellites in formation-flying to increase the resolution in the cross-track direction, the signal-to-noise ratio (SNR) and minimize clutter noise [5], while still maintaining the same performance and characteristics as the classical radar sounders in along-track direction. The orbits of individual satellites are selected so as to obtain a distribution of satellites spaced by a distance $d_{ct}$ in the cross-track direction, so that phased array beamforming techniques can be used. Considering a formation of $N$ satellites, uniformly distributed cross-track for a total length $L_{ct} = d_{ct}(N-1)$, the equivalent cross-track antenna half power beamwidth $\theta_b$ is equal to

$$\theta_b = \frac{\lambda}{L_{ct}} , \tag{27}$$

and the correspondent cross-track resolution is

$$R_{ct}^d = 0.886\,\theta_b\, h . \tag{28}$$

As in [5], it is possible to define the cross-track improvement resolution factor $IRF$, comparing the cross-track resolution of a single sounder and a distributed sounder

$$IRF(\theta_b) = \frac{R_{ct}^s}{R_{ct}^d} = \frac{2}{0.886\,\theta_b}\sqrt{\frac{c_0}{B_w h}} . \tag{29}$$

As can be deduced from Eq. (29), the improvement factor grows as the extension of the system in the cross-track direction $L_{ct}$ increases. Nevertheless, similarly to what seen in the along-track direction for a classical radar sounder, the maximum size must be limited to achieve coherent radiation.

$$\sqrt{\left(\frac{L_{ct}}{2}\right)^2 - h^2} - h \le \frac{\lambda}{4} , \tag{30}$$

and therefore, the maximum value of $L_{ct}$ is given by

$$L_{ct,max} = \sqrt{2\lambda h} . \tag{31}$$

By implementing the maximum $L_{ct} \equiv L_{ct,max}$, the minimum cross-track resolution and max IRF, for given altitude and wavelength are obtained as follows

$$R_{ct,max}^d = 0.886\sqrt{\frac{\lambda h}{2}} , \tag{32}$$

$$IRF^{d}_{ct,max} = \frac{2}{0.886}\sqrt{\frac{2c_o}{B_w \lambda}} \ . \tag{33}$$

For instance, by considering an altitude of $h = 500$ km and a wavelength range between HF and VHF (1 m $< \lambda <$ 100 m) the maximum achievable cross-track resolutions are:

$$R^{d}_{ct,max}(\lambda = 1\,\text{m}) = 443\ \text{m} \ , \tag{34}$$

$$R^{d}_{ct,max}(\lambda = 100\,\text{m}) = 4430\ \text{m} \ , \tag{35}$$

and the corresponding cross-track lengths needed to reach these resolutions are

$$L_{ct,max}(\lambda = 1\,\text{m}) = 1000\ \text{m} \ , \tag{36}$$

$$L_{ct,max}(\lambda = 100\,\text{m}) = 10\,000\ \text{m} \ . \tag{37}$$

If the relative distance between the phased array elements $d_{ct}$ is greater than the probing wavelength $\lambda$, electromagnetic waves produced by each element add constructively in other areas besides the main lobe, forming secondary lobes [42]. These secondary peaks, called grating lobes, are formed in the off-nadir direction for each $\theta$ that satisfies the following equation

$$2\pi \frac{d_{ct}}{\lambda}(\sin\theta - \sin\theta_0) = 2\pi p \ , \tag{38}$$

where $\theta_0$ indicates the pointing direction and $p \in \mathbb{Z}$. By considering a nadir pointing architecture ($\theta_0 = 0$), the angular position of the first ($p = 1$) grating lobe is

$$\theta_g = \sin^{-1}\left(\frac{\lambda}{d_{ct}}\right) . \tag{39}$$

To prevent grating lobes from folding into the scene and limit clutter noise, with reference to Fig. 2 it is possible to deduce the lower limit of the angular position of the first grating lobe

$$\theta_g \geq \cos^{-1}\left(\frac{h}{h + \sqrt{\varepsilon_r} z_p}\right) . \tag{40}$$

In summary, from the desired resolution $\theta_b$ we define the cross-track length of the system $L_{ct}$, while from the requirement on $\theta_g$ we define the distance between elements $d_{ct}$, and, as a consequence, the number of elements $N$ [5].

## 4. Tethered satellite systems as distributed radar sounder

This section introduces the model and method used to evaluate the performance of a tether satellite system used as a distributed radar sounder. Perturbations acting on the system are not considered. A nominal behavior is studied, under the assumption that the employed stabilization provides the desired effect, by maintaining the relative position between the satellites. First, the Cartesian Coordinate Systems (CCS) used for this analysis are introduced. Then, the geometric relationships that define the attitude of the tether and the position of the antenna elements placed along it are analyzed. Finally, the performances in terms of radar sounder are described, as a function of the system characteristics, and the problem of phase pointing is introduced.

### 4.1. Target acquisition geometry

The relative position of the antenna elements and the tether attitude are described in an orbital Cartesian Coordinate System. In particular, a Local Vertical-Local Horizontal (LVLH) CCS is used. This CCS is centered in the instantaneous center of mass (CoM) of the orbiting system, and has coordinate axes identified by the following unit vectors:

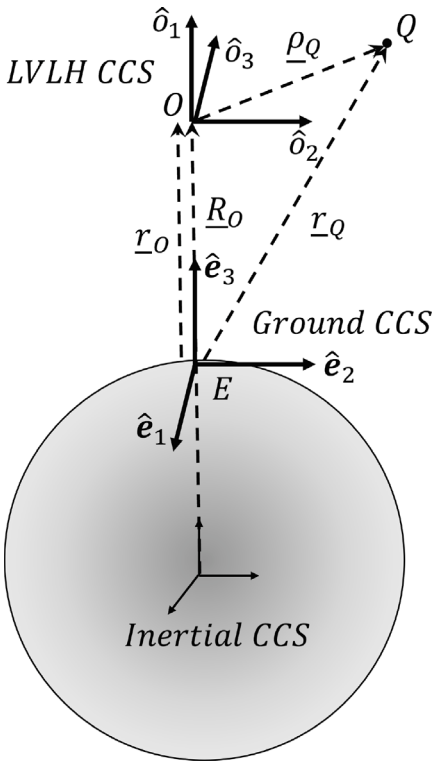


**Fig. 3.** Representation of the relationship between the introduced Cartesian Coordinate Systems.

- $\hat{o}_1 = \underline{R}_O / \|\underline{R}_O\|$ is pointed toward the instantaneous radial direction;
- $\hat{o}_3 = (\underline{R}_O \times \dot{\underline{R}}_O)/\|\underline{R}_O \times \dot{\underline{R}}_O\|$ is pointed toward the angular momentum vector (cross-track);
- $\hat{o}_2$ completes the right-hand triad $\hat{o}_2 = \hat{o}_3 \times \hat{o}_1$ (along-track).

Where vector $\underline{R}_O$ indicates the CoM with respect to the primary body center, and the dot is used to indicate time derivative with respect to the inertial frame. It is also crucial to introduce a ground CCS, so that the position of each point of the orbiting system can be easily described with respect to a point on the primary surface. This CCS is centered on the target $E$ and has coordinate axes identified by the following unit vectors:

- $\hat{e}_3$ is parallel and has the same direction as $\hat{o}_1$;
- $\hat{e}_2$ is parallel and has the same direction as $\hat{o}_2$;
- $\hat{e}_1$ completes the right-hand triad $\hat{e}_1 = \hat{e}_2 \times \hat{e}_3$.

The choice of orientation of the axes of this CCS has been made to coincide with the CCS used in [5]. Fig. 3 represents the CCSs introduced. Let us now consider a generic point Q, for which the following vector identity is valid

$$\underline{r}_Q = \underline{r}_O + \underline{\rho}_Q \ , \tag{41}$$

where vector $\underline{r}_Q$ is the position of point Q, with respect to the target, vector $\underline{r}_O$ is the position of the CoM O with respect to the target, and vector $\underline{\rho}_Q$ is the position of point Q with respect to the CoM. Since the integration time $T_i$ for the acquisition of a specific target $E$ is, in general, on the order of a tenth of a second, it is assumed that the motion of the LVLH CCS is rectilinear with constant velocity along $\hat{e}_2$, and therefore the two CCS remain parallel during the acquisition (Fig. 4). The evolution in time of the position of the center of the orbital CCS $O$ for a single observation can be easily calculated by making a few considerations. For a circular orbit and assuming a spherical primary body, the altitude $h$ is constant and the center of the orbital CCS, by

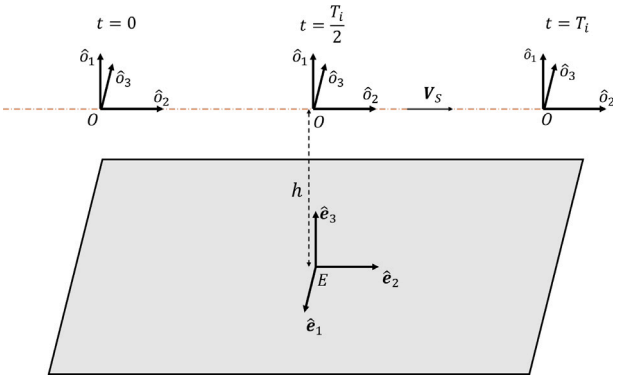


**Fig. 4.** Representation of the relationship between the ground CCS and the orbital during the acquisition of a specific target $E$.

definition, moves at the speed $V_s$ along the $\hat{o}_2$ direction, which coincides with $\hat{e}_2$. By considering that the acquisition starts at $t = 0$ and the target is at nadir when $t = T_i/2$ (Fig. 4), the evolution in time of the position of the center of the orbital CCS $O$ during an acquisition can be expressed in scalar components on the ground CCS as

$$\mathbf{r}_O^{GR} = \underline{r}_O \cdot \begin{Bmatrix} \hat{e}_1 \\ \hat{e}_2 \\ \hat{e}_3 \end{Bmatrix} = \begin{bmatrix} 0 \\ V_s(t - T_i/2) \\ h \end{bmatrix}^{GR} . \tag{42}$$

By projecting Eq. (41) in ground CCS, it yields

$$\mathbf{r}_Q^{GR} = \mathbf{r}_O^{GR} + C_{GO}\ \boldsymbol{\rho}_Q^O , \tag{43}$$

where $\mathbf{r}_Q^{GR}$ indicates the matrix of components of the vector $\underline{r}_Q$ in the ground CCS

$$\mathbf{r}_Q^{GR} = \underline{r}_Q \cdot \begin{Bmatrix} \hat{e}_1 \\ \hat{e}_2 \\ \hat{e}_3 \end{Bmatrix} . \tag{44}$$

$\boldsymbol{\rho}_Q^O$ indicates the matrix of components of the vector $\underline{\rho}_Q$ in the LVLH CCS

$$\boldsymbol{\rho}_Q^O = \underline{\rho}_Q \cdot \begin{Bmatrix} \hat{o}_1 \\ \hat{o}_2 \\ \hat{o}_3 \end{Bmatrix} , \tag{45}$$

and $C_{GO}$ is the Direction Cosine Matrix from the LVLH CCS to the ground CCS, given by

$$C_{GO} = \begin{bmatrix} 0 & 0 & -1 \\ 0 & 1 & 0 \\ 1 & 0 & 0 \end{bmatrix} . \tag{46}$$

### 4.2. Geometry of the tethered satellite system

Let us now consider a tether satellite system, with the tether being perfectly in tension along a rectilinear direction, identified by a unit vector $\hat{\imath}$. Let us then assume that the tether spans a total length $L$ and carries $N$ antenna elements. Those antenna elements are equally spaced along the tether, and the distance between any two of them is

$$d_p = \frac{L}{N-1} . \tag{47}$$

By considering the tether perfectly extended and stabilized, we can assume that it behaves like a rigid body for the sake of this analysis. Consequently, the distance between any two antenna elements remains constant in time, i.e.,

$$\frac{d(d_p)}{dt} = 0 . \tag{48}$$

Let us now define $\hat{f}$ as the unit vector along the projection of the unit vector $\hat{\imath}$ on the "along-track vertical plane", spanned by $\hat{o}_1$ and $\hat{o}_2$. The

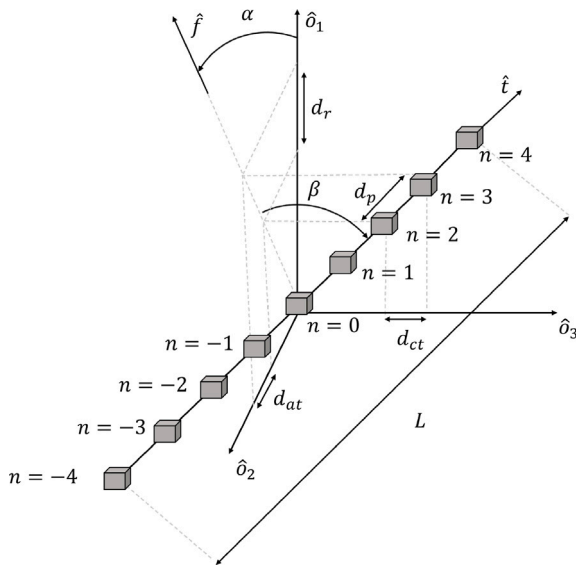


**Fig. 5.** Representation of a linear tethered satellite system composed of $N = 9$ antenna elements.

orientation of the tether with respect to the orbital CCS can be defined by using the following two angles: the "in-plane" angle $\alpha$ defined as the angle between $\hat{o}_1$ and $\hat{f}$ and the "out-of-plane" angle $\beta$ defined as the angle between $\hat{f}$ and $\hat{\imath}$ (see also Fig. 5). By projecting the distance $d_p$ onto the three unit vectors of the orbital CCS, the relative distance between two elements in the radial ($d_r$), along-track ($d_{at}$) and cross-track ($d_{ct}$) directions can be immediately computed as a function of the attitude of the tether, as

$$d_r = d_p \cos\beta \cos\alpha , \tag{49}$$

$$d_{at} = d_p \cos\beta \sin\alpha , \tag{50}$$

$$d_{ct} = d_p \sin\beta . \tag{51}$$

By using the notation introduced in [5], the antenna elements can be numbered with an index $n \in \mathbb{Z}$ such that

$$n = -\frac{N-1}{2}, \ \dots\ , \frac{N-1}{2} . \tag{52}$$

Therefore, notably, the coordinates of the generic antenna element $n$ in the LVLH CCS can be expressed as

$$\boldsymbol{\rho}_n^O = \underline{\rho}_n \cdot \begin{Bmatrix} \hat{o}_1 \\ \hat{o}_2 \\ \hat{o}_3 \end{Bmatrix} = \begin{bmatrix} n\ d_r \\ n\ d_{at} \\ n\ d_{ct} \end{bmatrix}^O . \tag{53}$$

By introducing Eqs. (49)–(51) into Eq. (53), it yields

$$\boldsymbol{\rho}_n^O = n\, d_p \begin{bmatrix} \cos\beta\ \cos\alpha \\ \cos\beta\ \sin\alpha \\ \sin\beta \end{bmatrix}^O . \tag{54}$$

The quantities and geometric relationships introduced are shown graphically in Fig. 5. By introducing Eq. (54) into Eq. (43), it is possible to obtain the position of a generic antenna element during a target acquisition, expressed in the ground CCS coordinates associated to that target, as a function of the tether attitude angles ($\alpha$, $\beta$).

### 4.3. Radar performance

Let us consider now that each antenna element, positioned along the tether, consists of an omnidirectional point-like sensor that transmits

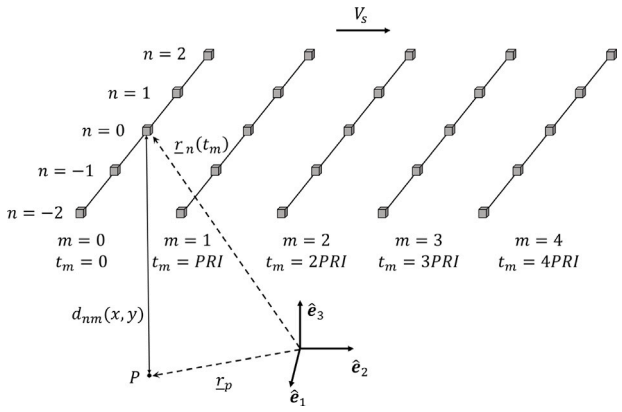


**Fig. 6.** Geometry of an acquisition for $N = 5$ and $N_{at} = 5$.

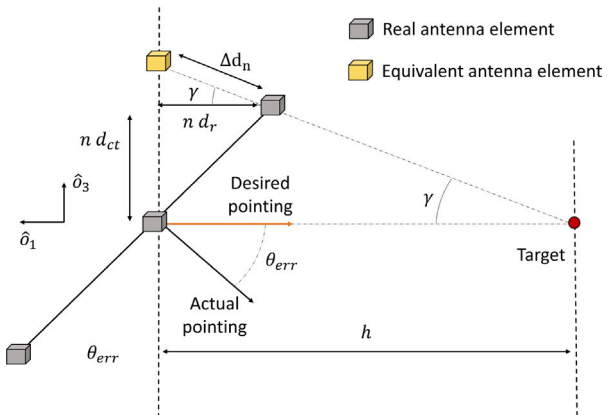


**Fig. 7.** Geometric sketch used for the phase correction $\Delta\phi_n$ computation.

and receives the signal with a probing frequency wavelength $\lambda$. This system forms a distributed radar sounder, whose cross-track equivalent antenna length ($L_{ct}$) is equal to the projection of the tether length $L$ on the cross-track direction $\hat{o}_3$

$$L_{ct} = L\,|\hat{t} \cdot \hat{o}_3| = L\,|\sin\beta| \ . \tag{55}$$

By substituting Eq. (55) in Eq. (27), it is possible to obtain the expression for the equivalent cross-track antenna beamwidth $\theta_b$ for a TSS

$$\theta_b = \frac{\lambda}{L_{ct}} = \frac{\lambda}{L|\sin\beta|} \ . \tag{56}$$

Similarly, the angular position of the first grating lobe can also be defined by combining Eqs. (51) and (39)

$$\begin{aligned}\theta_g &= \sin^{-1}\left(\frac{(N-1)\,\lambda}{L_{ct}}\right) \\ &= \sin^{-1}\left(\frac{\lambda}{d_p|\sin\beta|}\right) \ .\end{aligned} \tag{57}$$

Let us consider that each antenna element emits a pulse at regular instants, punctuated by the $PRI$ (pulse repetition interval), for a total of $N_{at}$ repetitions, while the system is moving along the along-track direction during an acquisition of a target $E$. The total number of pulses emitted by a single antenna element $N_{at}$ can be expressed as

$$N_{at} = \left\lfloor \frac{T_i}{PRI} \right\rfloor + 1 \ . \tag{58}$$

In Fig. 6, the geometry of a single acquisition of a target E is represented. Each of the $N$ antenna elements of the formation simultaneously emits a pulse, for a total of $N_{at}$ repetitions, as the system moves above the target. For an acquisition starting at $t = 0$, time can be discretized by performing the following parameterization

$$t_m = m\ PRI \ , \tag{59}$$

where

$$m = 0, 1, \ldots, N_{at} - 1 \ . \tag{60}$$

By denoting by $\underline{r}_n(t_m)$ the vector indicating the position of element $n$ at time $t_m$ relative to the target $E$, its projection in the ground CCS is

$$\mathbf{r}_{nm}^{GR} = \underline{r}_n(t_m) \cdot \begin{Bmatrix}\hat{e}_1 \\ \hat{e}_2 \\ \hat{e}_3\end{Bmatrix} = \begin{bmatrix}x_{nm} \\ y_{nm} \\ z_{nm}\end{bmatrix}^{GR} \ . \tag{61}$$

Now consider a generic point $P$ on the surface, whose position relative to the target is defined by the vector $\underline{r}_p$. Its projection in the ground CCS is

$$\mathbf{r}_P^{GR} = \underline{r}_p \cdot \begin{Bmatrix}\hat{e}_1 \\ \hat{e}_2 \\ \hat{e}_3\end{Bmatrix} = \begin{bmatrix}x \\ y \\ 0\end{bmatrix}^{GR} \ . \tag{62}$$

The distance between a generic point $P$ and the $n$-th antenna elements during the $m$-th pulse can be computed as

$$\begin{aligned}d_{nm}(x, y) &= \|\mathbf{r}_{nm}^{GR} - \mathbf{r}_P^{GR}\| \\ &= \sqrt{(x_{nm} - x)^2 + (y_{nm} - y)^2 + z_{nm}^2} \ .\end{aligned} \tag{63}$$

Given the assumption of omnidirectional pointlike sensors, the radiation emitted by the $n$-th antenna element during the $m$-th pulse on a generic point on the surface $P$ can be expressed as

$$\psi_{nm}(x, y) = \frac{A_{nm}}{d_{nm}(x, y)} e^{jkd_{nm}(x,y)} \ , \tag{64}$$

where $A_{nm}$ represents the amplitude of the signal, $k = 2\pi/\lambda$ is the wavenumber and $j$ is the imaginary unit. By assuming that each antenna element emits with identical initial phase, the total electric field on a generic point of the surface $\Psi(x, y)$ can be calculated by summing the contribution of all the $N$ antenna elements during $N_{at}$ pulses

$$\Psi(x, y) = \sum_n \sum_m \psi_{nm}(x, y) \ . \tag{65}$$

The relative two-way radiation intensity $U(x, y)$ can be computed as

$$U(x, y) = [\Psi(x, y)\Psi^{\dagger}(x, y)]^2 \ , \tag{66}$$

where the dagger symbol represents the Hermitian conjugate [5].

### 4.4. Phase pointing

If the tether lies on a plane parallel to the surface, using omnidirectional in-phase point-like sensors, a peak of the two-way radiation intensity is obtained at the center of the scene, corresponding to the target $E$. In case the tether lies on a plane not parallel to the surface, it is necessary to introduce a phase correction to ensure nadir pointing (Fig. 7). It is possible to define the pointing error $\theta_{err}$ as function of the attitude of the tether

$$\begin{aligned}\theta_{err} &= \tan^{-1}\left(\frac{n\ d_r}{n\ d_{ct}}\right) \\ &= \tan^{-1}\left(\frac{\cos\alpha}{\tan\beta}\right) \ .\end{aligned} \tag{67}$$

The phase correction can be calculated by considering an equivalent antenna element placed on a plane parallel to the ground (depicted in yellow in Fig. 7). The phase correction is equal to the wave number $k$ times the different line-of-sight distance with the target between the real and equivalent antenna element $\Delta d_n$. This, for a generic element $n$, can be defined as

$$\begin{aligned}\Delta\phi_n &= k\,\Delta d_n \\ &= k\left(-\frac{n\,d_r}{\cos\gamma}\right) \\ &\simeq -k(n\,d_p)\cos\beta\cos\alpha \ ,\end{aligned} \tag{68}$$

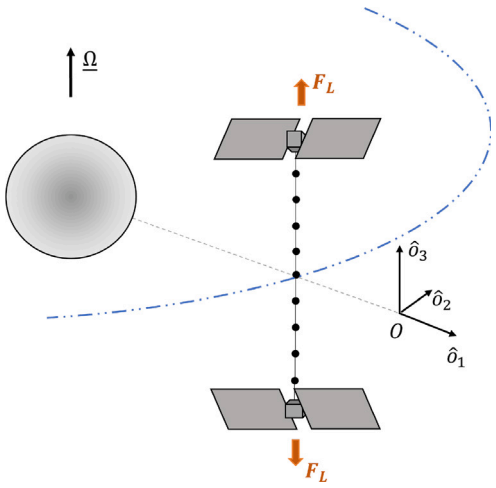


**Fig. 8.** Representation of an aerodynamically stabilized cross-track linear TSS.

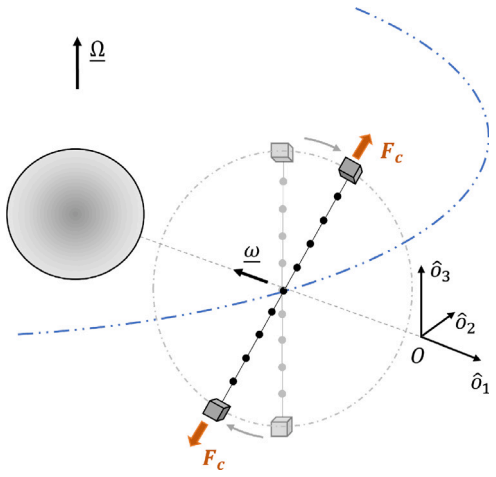


**Fig. 9.** Representation of a gyroscopically stabilized tether satellite system.

assuming that

$$\cos\gamma = \frac{h - n\ d_r}{\sqrt{(h - n\ d_r)^2 + (n\ d_{ct})^2}} \simeq 1\ . \tag{69}$$

The correction can be added in the function that describe the radiation emitted by the sensors

$$\psi_{nm}(x,y) = \frac{A_{nm}}{d_{nm}(x,y)} e^{jk[d_{nm}(t,x,y)+\Delta d_{nm}]}\ , \tag{70}$$

where

$$\begin{aligned}\Delta d_{nm} &= \Delta d_n(t_m) \\ &= -(n \cdot d_p)\cos\beta(t_m)\cos\alpha(t_m)\ ,\end{aligned} \tag{71}$$

whereas $\alpha$ and $\beta$ could change over time.

## 5. Aerodynamic stabilization of a linear TSS

The first architecture, studied in this paper, consists of a linear tether satellite system of the type described in Sec. 2.2, oriented along the cross-track direction. Due to the gravitational gradient, such a system would be naturally stable only in a radial configuration, i.e., with $\hat{t}$ parallel to $\hat{o}_1$ [43]. Here, as proposed in [16,17,44], aerodynamic surfaces are considered present at the extrema of the tether to maintain a stable cross-track configuration during the orbit. The lift ($F_L$) caused by the interaction with the rarefied atmosphere, assumed to exist around the primary body, provide the tension force in the tether. A representation of this system is shown in Fig. 8. This stabilization provides a constant aperture in the cross-track direction during the entire orbit, maximizing the performance of the system. Let assume that this kind of stabilization achieves a constant attitude of the tether, with the out-of-plane angle $\beta = 90°$. By substituting this value into Eqs. (49)–(51), it yields

$$d_r = 0\ , \tag{72}$$

$$d_{at} = 0\ , \tag{73}$$

$$d_{ct} = d_p\ . \tag{74}$$

And by substituting the value into Eq. (54), the position of a generic antenna elements $n$ in LVLH components yields

$$\boldsymbol{\rho}_n^O = \begin{bmatrix} 0 \\ 0 \\ n\ d_p \end{bmatrix}^O\ . \tag{75}$$

Due to the constant attitude, the characteristics of the system are constant over time

$$L_{ct} = L\ , \tag{76}$$

$$\theta_b = \frac{\lambda}{L}\ , \tag{77}$$

$$\theta_g = \sin^{-1}\left(\frac{\lambda}{d_p}\right)\ . \tag{78}$$

Moreover, since the tether stays parallel to the ground surface, pointing is not required, therefore,

$$\theta_{err} = 0\ . \tag{79}$$

## 6. Gyroscopic TSS

The second architecture, here studied, consists in a linear Tethered Satellite System that spins around its center of mass. The centrifugal force ($F_C$) caused by the rotation generate the tension force in the tether [15]. The angular momentum of the system (neglecting any perturbation) is fixed in the inertial frame, and its direction is chosen to be in the plane of the orbit, so as to maximize the performance for nadir-pointing observation. A representation of this system is shown in Fig. 9. This architecture does not need the atmosphere in order to be stabilized. Nevertheless, it cannot achieve a constant aperture in the cross-track direction during the orbit. For this reason, the remote sensing performance of this architecture changes continuously during the orbit. In particular, by considering a system rotating with an angular velocity vector, having magnitude $\omega$, direction equal to the unit vector $\hat{o}_2$ for $t = 0$, and opposite positive sense, it yields

$$\frac{d(\beta)}{dt} = \omega\ . \tag{80}$$

Furthermore, neglecting any perturbation torque, the angular momentum vector (or equivalently the angular velocity vector) will stay fixed in the inertial frame, and rotate in the LVLH frame with an angular rate $\Omega$

$$\frac{d(\alpha)}{dt} = -\Omega\ , \tag{81}$$

where

$$\Omega = \sqrt{\frac{\mu}{(R+h)^3}}\ . \tag{82}$$

By considering that for $t = 0$ the system is aligned in the radial direction $\hat{o}_1$ ($\beta = 0$, $\alpha = 0$), the in-plane and out-of-plane angles can be described as

$$\alpha(t) = -\Omega t\ , \tag{83}$$

**Table 3**
Data used for performance comparison.

| Parameter | Value | Unit |
|---|---|---|
| $\lambda$ | 6.66 | m |
| $B_w$ | 10 | MHz |
| $PRI$ | 2 | ms |
| $h$ | 500 | km |
| $z_p$ | 4 | km |
| $\epsilon_r$ | 3.1 | – |
| $R$ | 6372.79 | km |
| $\mu$ | $3.9860 \cdot 10^{14}$ | $m^3/s^2$ |

$$\beta(t) = \omega t \ . \tag{84}$$

The evolution of the distance between the antenna elements yields to be

$$d_r = d_p \cos(\omega t)\cos(-\Omega t) \ , \tag{85}$$

$$d_{at} = d_p \cos(\omega t)\sin(-\Omega t) \ , \tag{86}$$

$$d_{ct} = d_p \sin(\omega t) \ . \tag{87}$$

The position of a general element in LVLH components can be expressed as follows, by using Eq. (88),

$$\boldsymbol{\rho}_n^O = n\ d_p \begin{bmatrix} \cos(\omega t)\cos(-\Omega t) \\ \cos(\omega t)\sin(-\Omega t) \\ \sin(\omega t) \end{bmatrix}^O \ . \tag{88}$$

As a consequence, the remote sensing performances of the system are a function of time

$$L_{ct} = L|\sin(\omega t)| \ , \tag{89}$$

$$\theta_b = \frac{\lambda}{L|\sin(\omega t)|} \ , \tag{90}$$

$$\theta_g = \sin^{-1}\left(\frac{\lambda}{d_p|\sin(\omega t)|}\right) \ . \tag{91}$$

In this case, an active phase pointing is needed to compensate for the error

$$\theta_{err} = \tan^{-1}\left(\frac{\cos(-\Omega t)}{\tan(\omega t)}\right) \ . \tag{92}$$

## 7. Performance comparison

In this section the introduced tethered architectures are compared with the formation flying architecture proposed in [5] and a single sounder architecture, by analyzing the performance as an unfocused radar sounder. In order to evaluate the benefits brought purely by the satellite architecture, the same altitude, probing wavelength, bandwidth, PRI and penetration depth will be considered for all architectures, by supposing an acquisition of an icy subsurface on the Earth. The data used are summarized in Table 3 [5]. The same number of antenna elements is considered for all distributed systems, as computed here below. They are assumed to be spaced in such a way as to obtain an angular position of the first grating lobe and an equivalent cross-track beamwidth respectively equal to $\theta_g = 12.5°$, $\theta_b = 0.59°$. They are considered to be omnidirectional radiators. For all the architectures, the diameter of the scene is defined by Eq. (26)

$$D = \sqrt{(h + \sqrt{\epsilon_r} z_p)^2 - h^2} = 84215.9 \text{ m} \ . \tag{93}$$

This is represented as a black circle in the two-way radiation intensity contour plots. In the first part of this section we analyze the characteristics of the different architectures, then their resolution during an orbit is compared and, finally, the effect of array rotation angle on the gyroscopic TSS and the formation flying architectures is analyzed.

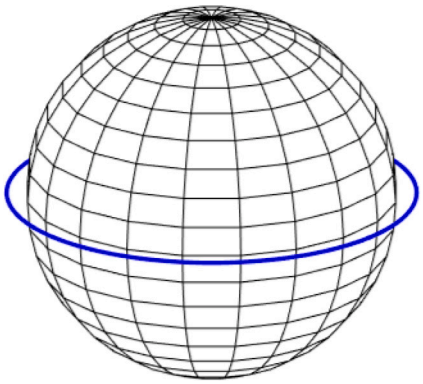

**Fig. 10.** Illustrative representation of trajectory followed by a single sounder architecture (not in scale).

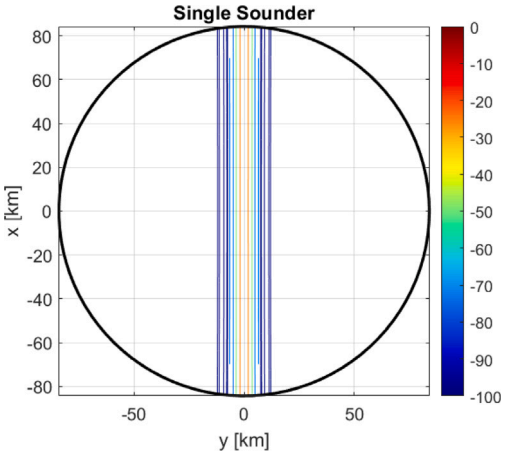


**Fig. 11.** Contour plot of the normalized two-way radiation intensity (in dB) for a single sounder architecture.

### 7.1. Single sounder

The simplest architecture consists in a single satellite ($N = 1$) orbiting along a circular orbit. In Fig. 10, an illustrative representation of the orbit followed by a single sounder is visualized. By using the equations introduced in Section 3 and the data of Table 3, it is possible to compute the performance of this architecture. For an unfocused Doppler focusing, the synthetic along-track aperture is equal to (Eq. (9))

$$L_{at}^{uf} = \sqrt{\frac{\lambda h}{2}} = 1290.3 \text{ m} \ . \tag{94}$$

As a consequence, the relative resolution in along-track is equal to (Eq. (18))

$$R_{at}^{uf} = \frac{\lambda h}{2L_{at}^{uf}} = 1290.3 \text{ m} \ . \tag{95}$$

Finally, the cross-track resolution is defined by Eq. (21)

$$R_{ct}^{s} = D_{pl} = 2\sqrt{\frac{h\, c_0}{B_w}} = 7745.9 \text{ m} \ . \tag{96}$$

The relative normalized two-way radiation pattern obtained for an acquisition is shown in Fig. 11. The figure shows that in the case of single sounder, the ground radiation assumes its maximum intensity throughout the strip about the straight line $y = 0$. As mentioned in Section 3, all electromagnetic waves incident on the scene are reflected and picked up by the sounder, generating clutter noise that deteriorate

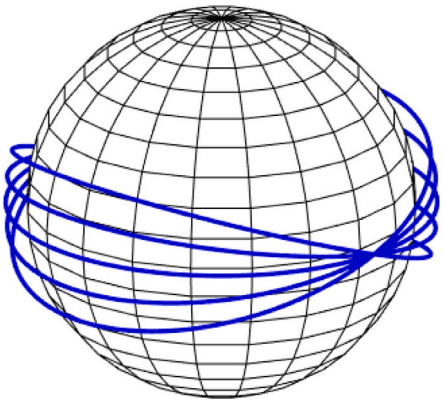

**Fig. 12.** Illustrative representation of trajectories followed by satellites in a formation flying architecture (not in scale).

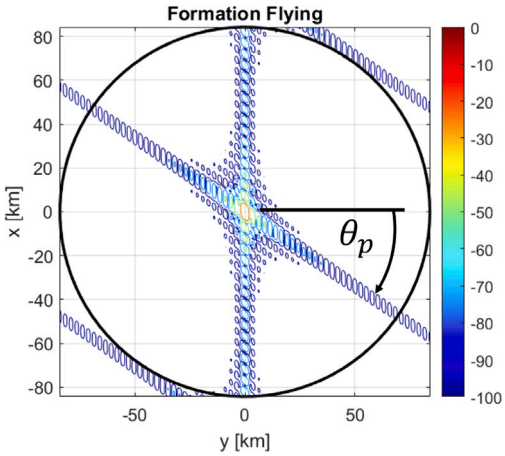


**Fig. 13.** Contour plot of the normalized two-way radiation intensity (in dB) for the formation flying architecture.

performance. The low directionality of the radiation in the cross-track direction greatly increases the possible clutter noise, limiting the acquisition accuracy of the system.

### 7.2. Formation flying

A formation flying architecture consists of multiple satellites orbiting along circular orbits, with different inclinations. Due specifically to the different inclination, the relative positions of the satellites vary during an orbit, and provides a maximum baseline in the cross-track direction only in two points along an orbit. Fig. 12 illustrates a formation flying architecture of $N = 5$ satellites. For an unfocused Doppler processing, the along track performance are the same of those computed for a single sounder:

$$L_{at}^{uf} = 1290.3 \text{ m} , \qquad R_{at}^{uf} = 1290.3 \text{ m} . \tag{97}$$

It is possible to compute the number of satellites $N$ and their spacing by considering the required characteristics of the phased array ($\theta_b$ and $\theta_g$). In order to obtain the equivalent cross-track beamwidth $\theta_b = 0.59°$, the distributed systems need to maximally extend in the cross-track direction for a total length of (Eq. (27))

$$L_{ct} = \frac{\lambda}{\theta_b} = 646.76 \text{ m} . \tag{98}$$

From the angular position of the first grating lobe $\theta_g = 11.5°$, the distance between the elements $d_{ct}$ and their number $N$ can be deduced (Eq. (39))

$$d_{ct} = \frac{\lambda}{\sin(\theta_g)} = 33.40 \text{ m} , \tag{99}$$

$$N = \frac{L}{d} + 1 = 21 . \tag{100}$$

Moreover, a displacement in the along track direction its needed in order to avoid a collision of the satellites where the orbit intersect:

$$d_{at} = 21.91 \text{ m} . \tag{101}$$

This displacement is obtained by considering the maximal array rotation angle $\theta_{p,max}$. More details are discussed in the next subsection. The cross-track resolution is computed by using Eq. (28)

$$R_{ct}^{ff} = 0.886\,\theta_b\,h = 4561.7 \text{ m} . \tag{102}$$

The relative cross-track improvement resolution factor is

$$IRF^{ff} = \frac{R_{ct}^{s}}{R_{ct}^{ff}} = 1.698 . \tag{103}$$

Finally, the relative normalized two-way radiation intensity pattern obtained for an acquisition is showed in Fig. 13 In this case, the distributed sounder focuses the radiation intensity on the center of the scene, greatly limiting clutter noise. The radiation pattern, in this case, is not parallel to the along-track direction ($y$), due to the effect of the array rotation angle $\theta_p$, described later. It is important to underline that, for formation flying architecture, the introduced performance are achieved only in the two points along the orbit, when the satellites span the largest distance in the cross-track direction.

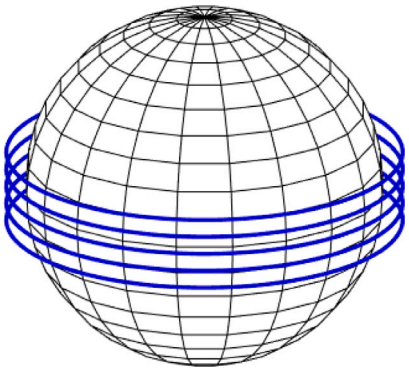

**Fig. 14.** Illustrative representation of trajectories followed by the elements of a cross-track aerodynamic stabilized tether satellite system (not in scale).

### 7.3. Aerodynamic TSS

The Tethered Satellite System architecture, with aerodynamic stabilization, ensures a constant cross-track distribution of the antenna elements, and, as a consequence, a constant cross-track length $L_{ct}$ during the entire orbit. Fig. 14 illustrates the orbits followed by the antenna elements of a cross-track tether architecture for radar sounding. Again, for an unfocused Doppler processing, the along track performance are the same of those computed for a single sounder:

$$L_{at}^{uf} = 1290.3 \text{ m} , \qquad R_{at}^{uf} = 1290.3 \text{ m} . \tag{104}$$

The number of elements $N$, the length of the tether $L$ and the distance between the element $d_p$ can be computed following the same procedures described before.

$$L = L_{ct} = 646.7 \text{ m}, \qquad N = 21, \qquad d_p = d_{ct} = 33.40 \text{ m} . \tag{105}$$

In this case, there is not any displacement in the along-track direction. The cross-track resolution and the IRF are equal to the previous case, but, this time, are preserved during the entire orbit

$$R_{ct}^{aTSS} = 4561.7 \text{ m} , \qquad IRF^{aTSS} = 1.698 . \tag{106}$$

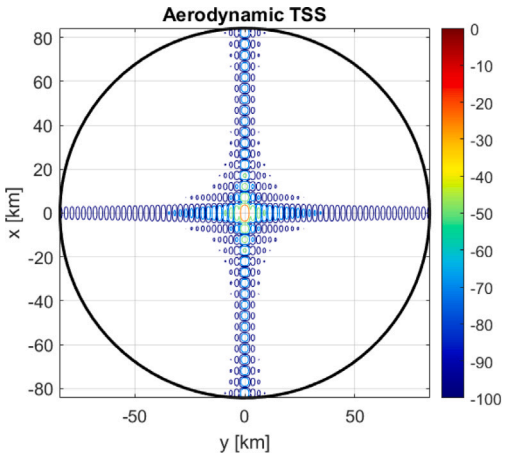


**Fig. 15.** Contour plot of the normalized two-way radiation intensity (in dB) for the aerodynamic TSS architecture.

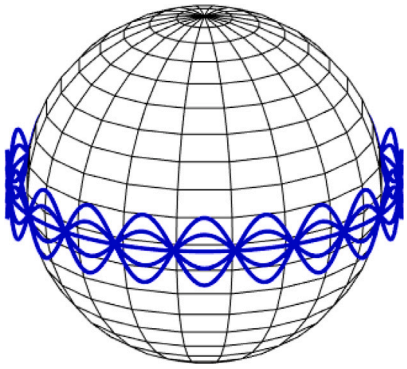

**Fig. 16.** Illustrative representation of trajectory followed by the elements of a gyroscopic stabilized tether (not in scale).

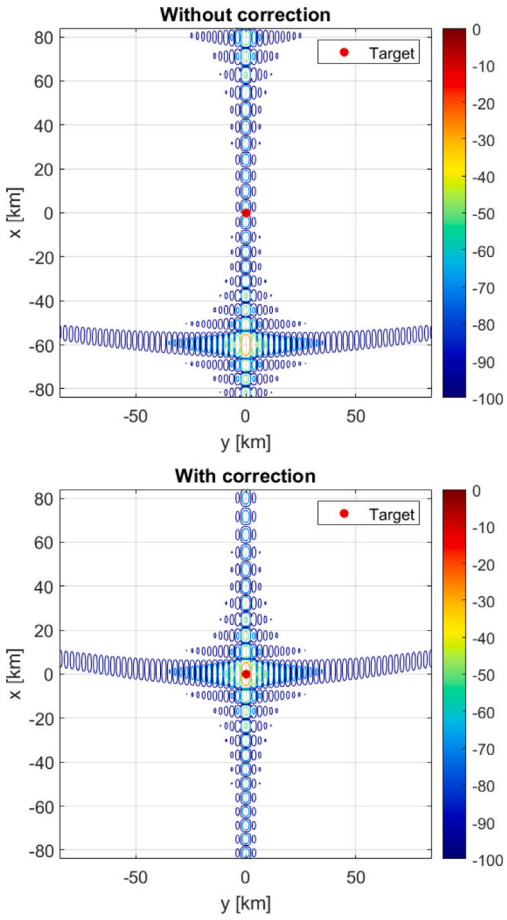


**Fig. 17.** Visualization of the effect of phase pointing on the contour plot of the normalized two-way radiation intensity on the surface in the case of a pointing error of $\theta_{err} = 45°$.

Finally, the relative normalized two-way radiation pattern obtained for an acquisition is showed in Fig. 15 This is the only architecture that keep the nominal radiation intensity pattern throughout the entire orbit. This is in fact focused only on the target, minimizing clutter noise, and the dynamics of the system allows this pattern to be maintained for each acquisition.

### 7.4. Gyroscopic TSS

The last architecture introduced uses gyroscopic effects in order to stabilize a linear tether. In this case, due to the rotation of the tether, the baseline is periodically changing with time according to the selected rotational speed. The maximum cross-track length is achieved in multiple points of the orbit. In Fig. 16, a representation of the orbits followed by the elements of a gyroscopic tether is visualized. Also in this case, the consideration done for the previous case are valid:

$$L_{at}^{uf} = 1290.3 \text{ m}\,, \qquad R_{at}^{uf} = 1290.3 \text{ m}\,, \tag{107}$$

$$L = 646.7 \text{ m}, \qquad N = 21, \qquad d_p = 33.40 \text{ m}\,. \tag{108}$$

However, due to the constant rotation of the tether, the performances continuously change during the orbit. By considering a stabilizing angular velocity $\omega = 0.01$ rad/s, we obtain:

$$R_{ct}^{gTSS} = min\left(\frac{4561.7 \text{ m}}{|\sin(0.01\,t)|},\ 7745.9 \text{ m}\right)\,, \tag{109}$$

$$IRF^{gTSS} = max\left(1.698|\sin(0.01\,t)|,\ 1\right)\,. \tag{110}$$

The *max* and *min* functions arise because, in case the antenna beamwidth is too low, the resolution would be equal to the first pulse-limited resolution cell, similarly to a single sounder case. For this architecture, the two-way radiation intensity pattern continuously changes during the orbit. The changes are due to two main effects. The first one is due to the array rotational angle $\theta_p$, that will be analyzed in a dedicated section, the second one is due to the pointing error $\theta_{err}$. By using the pointing technique introduced in Section 4, it is possible to counteract the effect of the $\theta_{err}$, and obtain a Nadir pointing radiation pattern in every point of the orbit. Fig. 17, shows the two-way radiation pattern for a $\theta_{err} = 45°$ ($\alpha = 90°$, $\beta = 45°$). The best and worst radiation intensity pattern achieved during the orbit will be respectively equal to the ones obtained with a cross-track TSS and a single sounder (Figs. 11, 15). The number of times the system reaches maximum amplitude ($N_{peak}$) during an orbit is calculated by considering the ratio of the period of the orbit to the period of the rotational motion of the tether

$$N_{peak} = 2\left\lfloor\frac{T_{orbit}}{T_{rotation}}\right\rfloor = 2\left\lfloor\frac{\omega}{\Omega}\right\rfloor\,. \tag{111}$$

For instance, in this case:

$$N_{peak} = 2\left\lfloor\frac{\omega}{\Omega}\right\rfloor = 18\,. \tag{112}$$

### 7.5. Cross-track resolution comparison

Now, let us analyze how the cross-track improvement resolution factor $IRF$ and the cross-track resolution change during an orbit

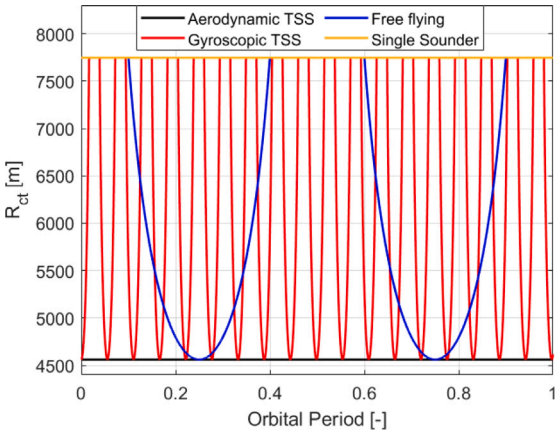


**Fig. 18.** Evolution of cross-track resolution $R_{ct}$ during an orbit for the four architectures.

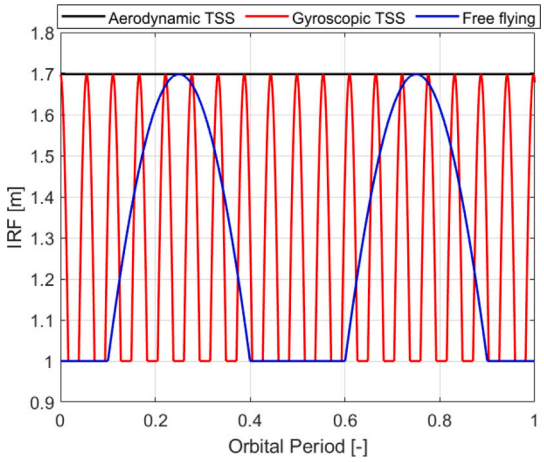


**Fig. 19.** Evolution of cross-track improvement resolution factor $IRF$ during an orbit for the three distributed architectures.

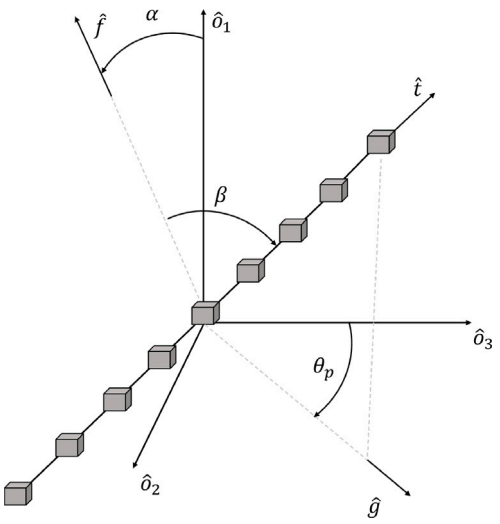


**Fig. 20.** Representation of the array rotational angle $\theta_p$ in the LVLH CCS.

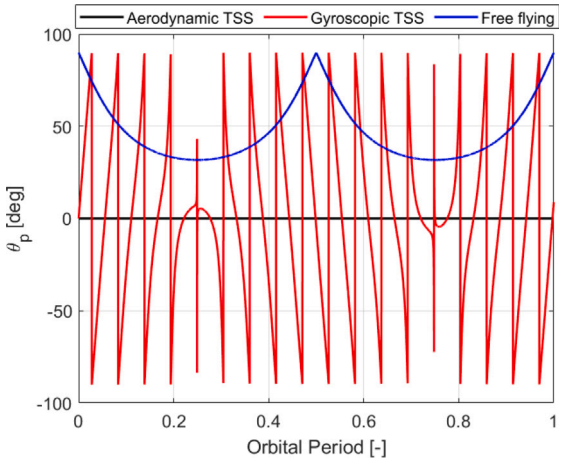


**Fig. 21.** Evolution of the rotational angle $\theta_p$ during an orbit for the three distributed architectures.

for the three distributed architectures (formation flight, aerodynamic, gyroscopic). As said before, the only distributed architecture that keeps the nominal characteristics during the entire orbit is the Aerodynamic TSS. Fig. 18 shows how the resolution of the three architectures change during an orbit. As a reference, also the single sounder resolution is plotted. In the same way, also the cross-track Improvement resolution factor can be obtained (Fig. 19). By using a tether it is possible to achieve the maximal cross-track resolution in more than two points during the orbit (up to the entire orbit for an aerodynamic TSS). These features are significantly superior to the formation flying case, making possible the acquisition of a much larger number of targets along the orbit.

### 7.6. Array rotation angle effects

The array rotation angle $\theta_p$ is the angle between the cross-track direction ($\hat{o}_3$) and the unit vector $\hat{g}$, obtained by projecting $\hat{t}$ on the plane defined by $\hat{o}_2$ and $\hat{o}_3$ (Fig. 20). For an Aerodynamic TSS $\theta_p$ is always equal to zero, but for a formation flying or gyroscopic tether architecture, it changes over time, and characterizes the radiation pattern on the surface. For a linear tether satellite system, $\theta_p$ can be defined as a function of tether attitude

$$\theta_p = \tan^{-1}\left(\frac{d_{at}}{d_{ct}}\right) = \tan^{-1}\left(\frac{\sin\alpha}{\tan\beta}\right). \tag{113}$$

For a formation flying architecture, the along-track distance between the elements ($d_{at}$) is constant, while the variation of the cross-track distance ($d_{ct}$) causes continuous variation of $\theta_p$, that reaches the minimum value when the system has the maximal extension in the cross-track direction. For this architecture it is not possible to achieve $\theta_p = 0$, since a certain distance between the satellites in the along-track direction is needed in order to avoid a collision when the orbits intersect [5]. Fig. 21 shows the evolution of $\theta_p$ for the three architectures during one orbit. Array rotation angle changes the radiation pattern on the surface, causing a rotation of the along-track pattern lines equal to $\theta_p$ (Fig. 25). For architectures based on formation flying satellites, it is necessary to limit the array rotation angle so that the grating lobes do not fold within the scene (i.e., peak ambiguity) [5]. Considering that the ground position of the first peak ambiguity is $h\tan\theta_g$, and that the array rotation angle causes an equal rotation of the radiation pattern, it is possible to calculate the maximum value of $\theta_p$ so that it does not fold inside the scene (Fig. 22)

$$\theta_{p,max} = \tan^{-1}\left[\sqrt{\left(\frac{h\tan\theta_g}{D}\right)^2 - 1}\right]. \tag{114}$$

In the case of a gyroscopic tethered system, it can be shown that the first grating lobes never fold in the scene under any attitude condition. In Eq. (57) we introduced how the angular position of the first grating

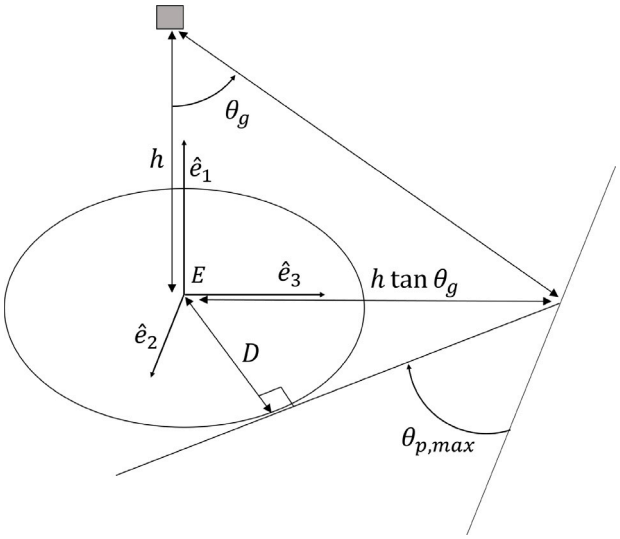


**Fig. 22.** Illustration of geometric considerations for obtaining $\theta_{p,max}$ (not in scale).

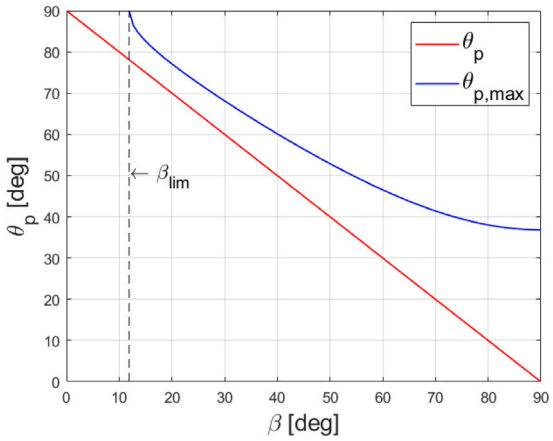


**Fig. 23.** Comparison of $\theta_{p,max}$ and $\theta_p$ for a tethered system. For any $\beta$ $\theta_p$ is smaller than $\theta_{p,max}$.

lobe depends on the attitude of the tether. Substituting in Eq. (114) we can obtain an expression of $\theta_{p,max}$ as a function of angle $\beta$

$$\theta_{p,max}(\beta) = \tan^{-1}\left[\sqrt{\left(\frac{\tan\left(\sin^{-1}\left(\frac{\lambda}{d_p|\sin\beta|}\right)\right)}{D/h}\right)^2 - 1}\right]. \tag{115}$$

At this point it is possible to compare the value of $\theta_{p,max}$ with that of $\theta_p$ as a function of attitude (Eq. (113)). In order to show that the condition is always satisfied, we consider the worst case ($\alpha = \pi/2$). In this case, as can be deduced from Fig. 21, we have

$$\theta_p = \frac{\pi}{2} - \beta\,. \tag{116}$$

In Fig. 23 the array rotation angle $\theta_p$ is compared with $\theta_{p,max}$ for different values of $\beta$. The plot is limited to values of $0° \le \beta \le 90°$, but given the symmetry of the system, the concept is extendable to any value of $\beta$. Interestingly, for values less than $\beta_{lim} = sin^{-1}\left(\frac{\lambda}{d_p}\right)$, $\theta_{p,max}$ is not defined.

This is because, in these cases, the cross-track distance between antenna elements is less than or equal to the probing wavelength $\lambda$, and, as a consequence, no grating lobes will be generated. Nevertheless, although acquisitions can be made with any array rotation angle, the decrease in cross-track distance causes a lowering of the resolution. In Fig. 24 it is

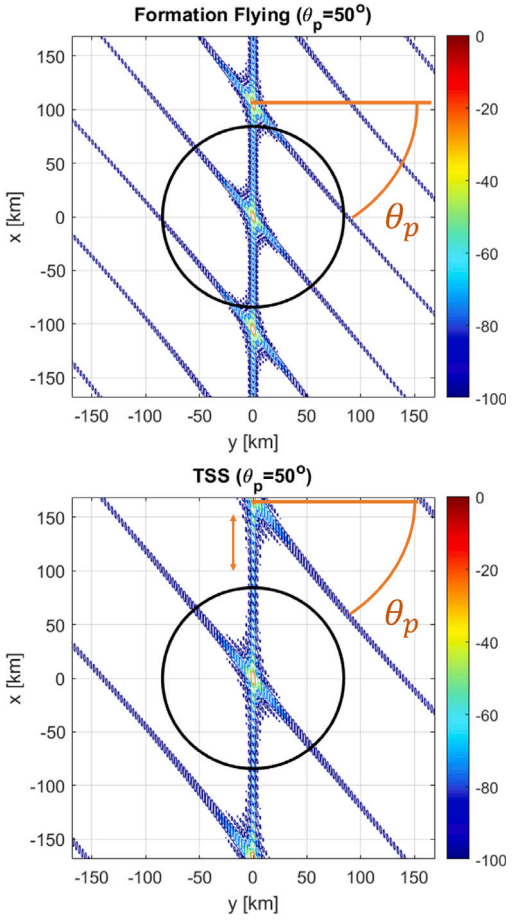


**Fig. 24.** Comparison of the effect of high array rotation angle ($\theta_p$) on the contour plot of the normalized two-way radiation intensity on the surface for a formation flying architecture and a TSS.

possible to see that for a formation flying architecture the grating lobe falls into the useful sounding scene (represented as a black circle) for $\theta_p = 50°$, while the peak ambiguity is avoided for a tethered system. In Figs. 25 and 26 the effects of different $\theta_p$ angle on the two-way radiation intensity pattern on the surface is visualized, respectively for a gyroscopic tether and a formation flying architecture.

## 8. Discussion

In light of the analysis performed above, it is possible to discuss the characteristics and performance of the radar sounder architectures presented. By using an architecture with formation flying satellites, it is possible to obtain acquisitions of the desired quality only at a few points along the orbit. By performing an optimization of orbit characteristics, it is possible to obtain up to a maximum of four acquisition points, if they do not coincide with the maximum cross-track aperture, and only two if maximum cross-track resolution is desired. The use of a tether system enables to maintain the relative position between the antenna elements with high accuracy. Moreover, the antenna elements placed along the tether are much simpler and cheaper than an entire satellite. The aerodynamic stabilized tether achieves the best performance in radar remote sensing applications. Its maximum aperture stays constant during the entire orbit, enabling to perform target acquisition in every moment, at the maximum cross-track resolution. Furthermore, since the system require the rarefied atmosphere of very low orbit, this kind of system would typically operate at lower altitude, increasing even more the ground resolution. Nevertheless, due to aerodynamic drag caused

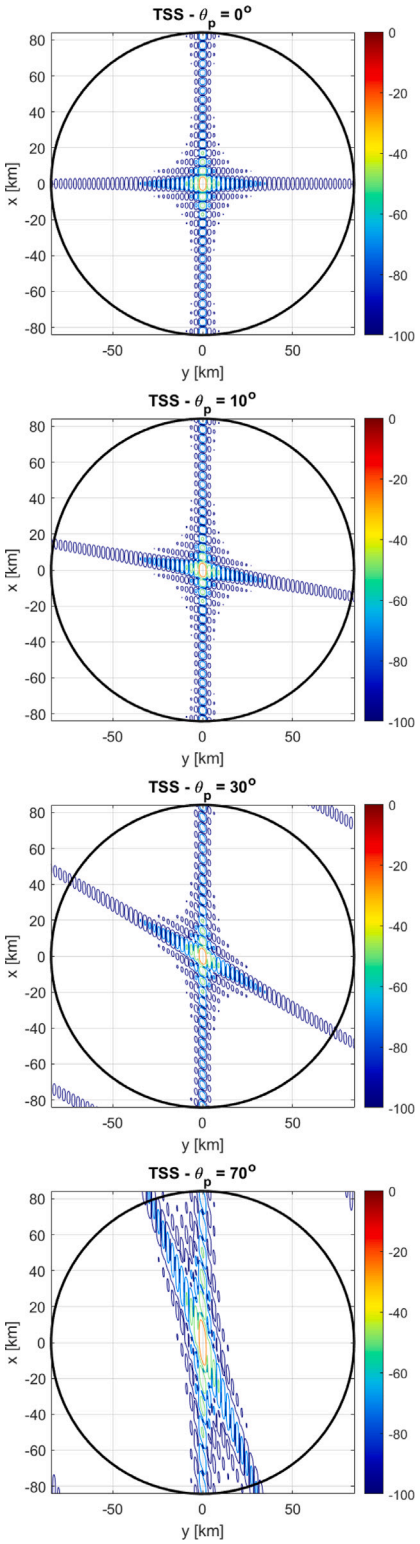


**Fig. 25.** Effect of the array rotation angle $\theta_p$ on the ground normalized two-way radiation intensity generated by a gyroscopic tether architecture.

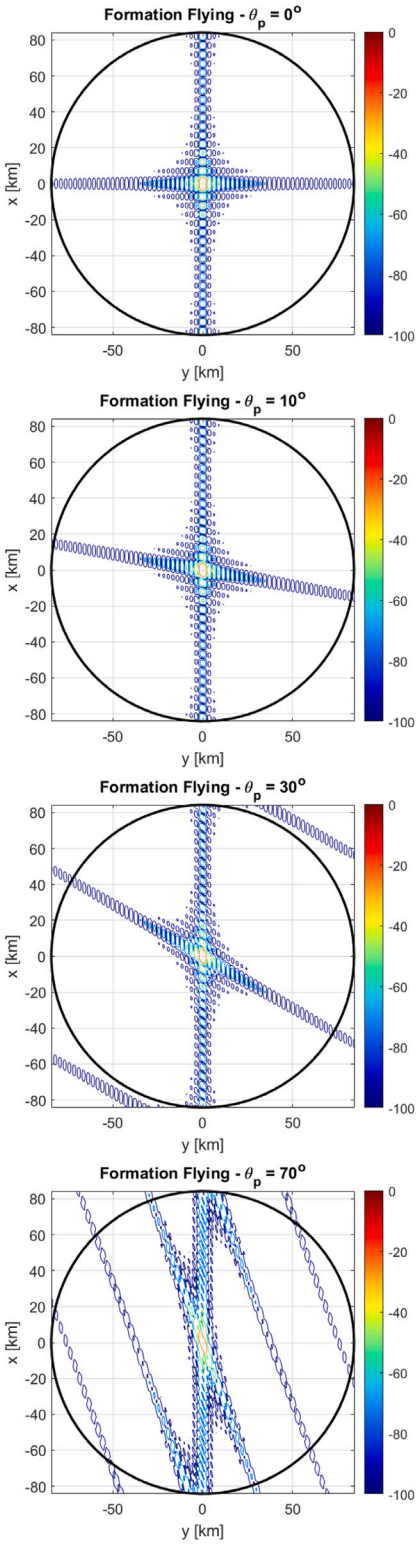


**Fig. 26.** Effect of the array rotation angle $\theta_p$ on the ground normalized two-way radiation intensity generated by a formation flying architecture.

by the stabilizing surfaces, frequent orbital maneuvers are needed in order to keep the orbit altitude [16]. The gyroscopically stabilized tether, on the other hand, can perform multiple acquisition per orbit with maximum cross-track resolution. The phase pointing technique, here proposed, in combination with the effect of the tether that avoids the peak ambiguity, allows lower cross-track resolution acquisitions throughout the entire orbit. The choice between these architectures will strongly depend on the specific requirements of the mission. The aerodynamic architecture is well suited to missions where the target is not well defined in advance (such as on-demand remote sensing).

Formation flying is appropriate only when mission targets are few and well identified. Finally, the gyroscopic stabilization is particularly suitable for missions that require monitoring of multiple well-defined targets, being able to optimize the architecture as needed.

## 9. Conclusions

In this paper two tether satellite systems architectures are proposed for radar sounder application: the first is maintained in cross-track by using aerodynamic surfaces while the second one is stabilized by gyroscopic effects. By placing the antenna elements on a tether stabilized with the techniques previously studied by the authors, it is possible to use Synthetic Aperture Radar techniques to synthesize a large antenna, providing performance not achievable with monolithic satellites. In addition, thanks to the mechanical link provided by the tether, it is possible to greatly simplify the satellites placed on it, decreasing costs compared to a free-flying formation flying architecture. After introducing the methodology to describe system performances as a function of tether attitude, the two stabilization techniques were introduced, highlighting their major characteristics. From the dynamics describing the nominal behavior of these systems, their performance during an orbit was calculated and compared with that of a formation flying system presented in a previous study. This analysis revealed that both tether architectures minimize clutter noise. In addition, the tether system stabilized with aerodynamic surfaces achieves maximum cross-track resolution throughout the entire orbit. The gyroscopic tether system, on the other hand, is able to achieve maximum performance at different points in the orbit, depending on the stabilization angular velocity, and can be used continuously with variable resolution. Notably, many open questions remain regarding the feasibility, mission and system design of aerodynamically stabilized tether satellite systems. Some of those questions are subject of ongoing investigations by the authors.

## CRediT authorship contribution statement

**Stefano Aliberti:** Conceptualization, Formal analysis, Investigation, Software, Validation, Writing – original draft, Writing – review & editing. **Marco B. Quadrelli:** Writing – review & editing. **Marcello Romano:** Invention of the cross-track tethered satellite systems, Research concept and strategy, Supervision, Writing – review & editing.

## Declaration of competing interest

The authors declare that they have no known competing financial interests or personal relationships that could have appeared to influence the work reported in this paper.

## Acknowledgments

Dr. Romano acknowledges the contribution of Fondazione Compagnia di San Paolo pertaining to the grant titled ‘Advanced Space System Engineering to Address Broad Societal Benefits’. Dr. Quadrelli’s contribution was carried out at the Jet Propulsion Laboratory, California Institute of Technology, under a contract with the National Aeronautics and Space Administration (80NM0018D0004), as part of the JPL Visiting Student Research Program that hosted Mr. Aliberti under the mentorship of Dr. Quadrelli. This paper contains significant new information with respect to the initial work performed by Mr. Aliberti during the internship with JPL under the supervision of Dr. Quadrelli. In particular, the methods for the stabilization of a cross-track tether satellite system by sole use of aerodynamic surfaces or gyroscopic effects, and the use of these architectures for radar sounding missions, are new concepts developed after Mr. Aliberti in November 2022 became a Ph.D. candidate at Politecnico di Torino, under the advisorship of Prof. Marcello Romano.

## References

[1] L. Bruzzone, G. Alberti, C. Catallo, A. Ferro, W. Kofman, R. Orosei, Subsurface radar sounding of the jovian moon ganymede, Proc. IEEE 99 (5) (2011) 837–857, http://dx.doi.org/10.1109/JPROC.2011.2108990.

[2] L.J. Porcello, R.L. Jordan, J.S. Zelenka, G.F. Adams, R.J. Phillips, W.E. Brown, S.H. Ward, P.L. Jackson, The apollo lunar sounder radar system, Proc. IEEE 62 (6) (1974) 769–783, http://dx.doi.org/10.1109/PROC.1974.9517.

[3] G. Picardi, D. Biccari, A. Bazzoni, F. Fois, M. Iorio, R. Seu, P. Melacci, C. Federico, A. Frigeri, G. Minelli, L. Marinangeli, R. Orosei, D. Calabrese, E. Zampolini, W.T.K. Johnson, R.L. Jordan, J. Plaut, A. Safaenili, Mars advanced radar for subsurface and ionosphere sounding (MARSIS): subsurface performances evaluation, in: 2003 Proceedings of the International Conference on Radar (IEEE Cat. No. 03EX695), 2003, pp. 515–521, http://dx.doi.org/10.1109/RADAR.2003.1278795.

[4] S. Sasaki, Y. Iijima, K. Tanaka, M. Kato, M. Hashimoto, H. Mizutani, Y. Takizawa, The SELENE mission: Goals and status, Adv. Space Res. 31 (11) (2003) 2335–2340, http://dx.doi.org/10.1016/S0273-1177(03)00543-X.

[5] L. Carrer, C. Gerekos, F. Bovolo, L. Bruzzone, Distributed radar sounder: A novel concept for subsurface investigations using sensors in formation flight, IEEE Trans. Geosci. Remote Sens. 57 (12) (2019) 9791–9809, http://dx.doi.org/10.1109/TGRS.2019.2929422.

[6] R. Apa, M.B. Quadrelli, R.M. Beauchamp, Dynamics and control of helical arrays in low earth orbit, in: 2022 IEEE Aerospace Conference, AERO, 2022, pp. 1–20, http://dx.doi.org/10.1109/AERO53065.2022.9843283.

[7] A. Moccia, S. Vetrella, A tethered interferometric synthetic aperture radar (SAR) for a topographic mission, IEEE Trans. Geosci. Remote Sens. 30 (1) (1992) 103–109, http://dx.doi.org/10.1109/36.124220.

[8] A. Moccia, S. Vetrella, M. Grassi, Attitude dynamics and control of a vertical interferometric radar tethered altimeter, J. Guid. Control Dyn. 16 (2) (1993) 264–269, http://dx.doi.org/10.2514/3.20998.

[9] M.S. Haynes, R.M. Beauchamp, A. Khazendar, R. Mazouz, M.B. Quadrelli, P. Focardi, R.E. Hodges, W. Bertiger, N. Bienert, Debris: Distributed element beamformer radar for ice and subsurface sounding, in: 2021 IEEE International Geoscience and Remote Sensing Symposium IGARSS, 2021, pp. 651–654, http://dx.doi.org/10.1109/IGARSS47720.2021.9554746.

[10] R. Mazouz, M.B. Quadrelli, R.M. Beauchamp, Dynamics and optimal control for free-flight and tethered arrays in low earth orbit, in: 2021 IEEE Aerospace Conference (50100), 2021, pp. 1–20, http://dx.doi.org/10.1109/AERO50100.2021.9438513.

[11] B.S. Yu, Z.H. Zhu, Symmetric and asymmetric dynamics of a tethered satellite in nontypical planes, Acta Astronaut. (ISSN: 0094-5765) 202 (2023) 585–594, http://dx.doi.org/10.1016/j.actaastro.2022.11.019.

[12] M.B. Quadrelli, E.C. Lorenzini, Dynamics and stability of a tethered centrifuge in low earth orbit, J. Astronaut. Sci. 40 (1992).

[13] G.B. Palmerini, S. Sgubini, M. Sabatini, Space webs based on rotating tethered formations, Acta Astronaut. 65 (1) (2009) 131–145, http://dx.doi.org/10.1016/j.actaastro.2009.01.056.

[14] B.S. Yu, K. Ji, Z.T. Wei, D.P. Jin, In-plane global dynamics and ground experiment of a linear tethered formation with three satellites, Nonlinear Dynam. 108 (4) (2022) 3247–3278, http://dx.doi.org/10.1007/s11071-022-07403-9.

[15] S. Aliberti, M.B. Quadrelli, M. Romano, Dynamics and control of gyroscopic stabilized tether satellite system in LEO, in: International Astronautical Conference, Baku, Azerbaijan, 2023.

[16] S. Aliberti, M.B. Quadrelli, M. Romano, Dynamics and aerodynamic control of a cross-track tether satellite system, in: ESA GNC & ICATT Conference 2023, 2023.

[17] M. Romano, S. Aliberti, R. Apa, C.L. Matonti, Metodo ed apparato per la stabilizzazione di formazioni di satelliti, 2023, Patent pending.

[18] H.M. Braun, F. Merkle, The new german high-resolution SAR reconnaissance system started its 10-year operations, in: Sensors and Systems for Space Applications III, Vol. 7330, 2009, pp. 9–14, http://dx.doi.org/10.1117/12.817521.

[19] F. Covello, F. Battazza, A. Coletta, E. Lopinto, C. Fiorentino, L. Pietranera, G. Valentini, S. Zoffoli, COSMO-SkyMed an existing opportunity for observing the earth, J. Geodyn. 49 (3) (2010) 171–180, http://dx.doi.org/10.1016/j.jog.2010.01.001.

[20] S. Ochs, W. Pitz, The TerraSAR-X and TanDEM-X satellites, in: 2007 3rd International Conference on Recent Advances in Space Technologies, 2007, pp. 294–298, http://dx.doi.org/10.1109/RAST.2007.4283999.

[21] J. Sanchez Palma, A. Solana Gonzalez, I. Martin Hervas, F. Monjas Sanz, M. Labriola, J. Martinez Cengotitabengoa, F.M. Garcia Molleda, S. Moreno Aguado, P. Saameno Perez, J. Closa Soteras, V. Bautista Juzgado, SAR panel design and performance for the PAZ mission, in: 8th European Conference on Synthetic Aperture Radar, 2010, pp. 1–4.

[22] V. Kerbaol, B. Chapron, P.W. Vachon, Analysis of ERS-1/2 synthetic aperture radar wave mode imagettes, J. Geophys. Res.: Oceans 103 (C4) (1998) 7833–7846, http://dx.doi.org/10.1029/97JC01579.

[23] K.C. Jezek, RADARSAT-1 antarctic mapping project: change-detection and surface velocity campaign, Ann. Glaciol. 34 (2002) 263–268, http://dx.doi.org/10.3189/172756402781818030.

[24] R. Girard, P.F. Lee, K. James, The RADARSAT-2/3 topographic mission: an overview, in: IEEE International Geoscience and Remote Sensing Symposium, Vol. 3, 2002, pp. 1477–1479, http://dx.doi.org/10.1109/IGARSS.2002.1026154, vol.3.

[25] A.A. Thompson, Overview of the RADARSAT constellation mission, Can. J. Remote Sens. 41 (5) (2015) 401–407, http://dx.doi.org/10.1080/07038992.2015.1104633.

[26] Z. Run-ning, J. Xiu-peng, System design and in-orbit verification of the HJ-1-C SAR satellite, J. Radars 3 (13135) (2014) 249, http://dx.doi.org/10.3724/SP.J.1300.2014.13135.

[27] R.L. Jordan, The seasat-a synthetic aperture radar system, IEEE J. Ocean. Eng. 5 (2) (1980) 154–164, http://dx.doi.org/10.1109/JOE.1980.1145451.

[28] A. Rosenqvist, M. Shimada, B. Chapman, K. McDonald, G. De Grandi, H. Jonsson, C. Williams, Y. Rauste, M. Nilsson, D. Sango, M. Matsumoto, An overview of the JERS-1 SAR global boreal forest mapping (GBFM) project, in: IGARSS 2004. 2004 IEEE International Geoscience and Remote Sensing Symposium, Vol. 2, 2004, pp. 1033–1036, http://dx.doi.org/10.1109/IGARSS.2004.1368587, vol.2.

[29] A. Rosenqvist, M. Shimada, N. Ito, M. Watanabe, ALOS PALSAR: A pathfinder mission for global-scale monitoring of the environment, IEEE Trans. Geosci. Remote Sens. 45 (11) (2007) 3307–3316, http://dx.doi.org/10.1109/TGRS.2007.901027.

[30] T.L. Toan, S. Quegan, M.W.J. Davidson, H. Balzter, P. Paillou, K. Papathanassiou, S. Plummer, F. Rocca, S. Saatchi, H. Shugart, L. Ulander, The BIOMASS mission: Mapping global forest biomass to better understand the terrestrial carbon cycle, Remote Sens. Environ. 115 (11) (2011) 2850–2860, http://dx.doi.org/10.1016/j.rse.2011.03.020.

[31] L. Bruzzone, J.J. Plaut, G. Alberti, D.D. Blankenship, F. Bovolo, B.A. Campbell, D. Castelletti, Y. Gim, A.M. Ilisei, W. Kofman, G. Komatsu, W. McKinnon, G. Mitri, A. Moussessian, C. Notarnicola, R. Orosei, G.W. Patterson, E. Pettinelli, D. Plettemeier, Jupiter ICY moon explorer (JUICE): Advances in the design of the radar for icy moons (RIME), in: 2015 IEEE International Geoscience and Remote Sensing Symposium, IGARSS, 2015, http://dx.doi.org/10.1109/IGARSS.2015.7326002.

[32] L. Bruzzone, F. Bovolo, S. Thakur, L. Carrer, E. Donini, C. Gerekos, S. Paterna, M. Santoni, E. Sbalchiero, Envision mission to venus: Subsurface radar sounding, in: IGARSS 2020 - 2020 IEEE International Geoscience and Remote Sensing Symposium, 2020, pp. 5960–5963, http://dx.doi.org/10.1109/IGARSS39084.2020.9324279.

[33] R. Seu, D. Biccari, R. Orosei, L. Lorenzoni, R. Phillips, L. Marinangeli, G. Picardi, A. Masdea, E. Zampolini, SHARAD: The MRO 2005 shallow radar, Planet. Space Sci. 52 (1) (2004) 157–166, http://dx.doi.org/10.1016/j.pss.2003.08.024.

[34] R.L. Jordan, B.L. Huneycutt, M. Werner, The SIR-C/X-SAR synthetic aperture radar system, IEEE Trans. Geosci. Remote Sens. 33 (4) (1995) 829–839, http://dx.doi.org/10.1109/36.406669.

[35] M. Werner, Shuttle radar topography mission (SRTM) mission overview, Frequenz 55 (3–4) (2001) 75–79, http://dx.doi.org/10.1515/FREQ.2001.55.3-4.75.

[36] J. Louet, S. Bruzzi, ENVISAT mission and system, in: IEEE 1999 International Geoscience and Remote Sensing Symposium. IGARSS'99 (Cat. No.99CH36293), Vol. 3, 1999, pp. 1680–1682, http://dx.doi.org/10.1109/IGARSS.1999.772059, vol.3.

[37] T. Ono, H. Oya, Lunar radar sounder (LRS) experiment on-board the SELENE spacecraft, Earth Planets Space 52 (9) (2000) 629–637, http://dx.doi.org/10.1186/BF03351671.

[38] S.-R. Lee, Overview of KOMPSAT-5 program, mission, and system, in: 2010 IEEE International Geoscience and Remote Sensing Symposium, 2010, pp. 797–800, http://dx.doi.org/10.1109/IGARSS.2010.5652759.

[39] T. Misra, A.S. Kirankumar, RISAT-1: Configuration and performance evaluation, in: 2014 XXXIth URSI General Assembly and Scientific Symposium, URSI GASS, 2014, pp. 1–4, http://dx.doi.org/10.1109/URSIGASS.2014.6929612.

[40] P. Potin, P. Bargellini, H. Laur, B. Rosich, S. Schmuck, Sentinel-1 mission operations concept, in: 2012 IEEE International Geoscience and Remote Sensing Symposium, 2012, pp. 1745–1748, http://dx.doi.org/10.1109/IGARSS.2012.6351183.

[41] Y. Kankaku, S. Suzuki, Y. Osawa, ALOS-2 mission and development status, in: 2013 IEEE International Geoscience and Remote Sensing Symposium - IGARSS, 2013, pp. 2396–2399, http://dx.doi.org/10.1109/IGARSS.2013.6723302.

[42] R.J. Mailloux, Phased Array Antenna Handbook, Artech house, 2017.

[43] J. Ashenberg, C. Lorenzini, Active gravity-gradient stabilization of a satellite in elliptic orbits, Acta Astronaut. (ISSN: 0094-5765) 45 (10) (1999) 619–627, http://dx.doi.org/10.1016/S0094-5765(99)00127-7.

[44] A.D. Ogundele, M. Romano, Dynamics and Control of A Cross-Track-Lift (CTRL) Tethered Spacecraft System, Technical Report, Spacecraft Robotics Laboratory, Naval Postgraduate School, Monterey, California, 93940, 2019.